LUND UNIVERSITY
Faculty of Science

Time-Resolved Diagnostic of Electrode Erosion in Spark Plugs

Ruike Bi

Thesis submitted for the degree of Master of Science
Project duration: 8 months

Supervised by Mattias Richter and Andreas Ehn

Department of Physics
Division of Combustion Physics
May 2019

Abstract

The short lifetime of spark plugs in heavy-duty truck and stationary engines has been a major concern in the relevant industry. In this thesis work a time-resolved approach to detect the evaporation erosion of Ni electrodes in electrical discharges was proposed, and multiple detection methods were used to study the spark discharge. Spectroscopic study of the discharge's emission illustrated the existence of the Ni atomic lines in the spectral range of 338 nm to 355 nm. Spectra also reported randomness in both the appearance of the Ni signal and the position where the signal is recorded. Based on the spectral measurement, it was proposed that a photomultiplier tube and a 10-nm-bandwidth band-pass filter centered at 343 nm can be used to investigate the temporal behavior of the Ni emission during one discharge, which can in principle reflect the erosion rate of the Ni electrode. The results reported a rapid rise in Ni emission at the beginning of the discharge. In the photomultiplier tube signal profiles, a stochastic behavior was also observed, in both the temporal width and the timing of the emission peaks. The effect of different parameters and spark modes on the erosion rate of Ni electrodes was studied statically. It was found that the erosion of the electrodes scales up almost linearly with the coil charging time; no clear correlation was observed between electrode erosion and cross flow speed or repetition rate of the discharge. In a capacitive system, it was found that the Ni electrode suffers more erosion when acting as the anode and that AC discharges do less erosion than DC ones. Finally, the morphology of new and worn electrodes was compared using a self-built macro imaging system.

Acknowledgements

I would like to express my gratitude to my supervisors, Mattias Richter and Andreas Ehn, for their kind instruction and strong support through the whole process of this thesis work. And I'd like to thank Jakob Ängeby, Tomas Karlsson and Lars-Åke Andersson from SEM AB for the proposing of this project and all the help in the process.

I wish to also thank everyone in the Division of Combustion Physics, especially Alexios Matamis, David Sanned, Christian Binder, Henrik Feuk, Panagiota Stamatoglou, Saeed Derafshzan and Zhenkan Wang, for not only the support in the thesis but also the enjoyable moments I had in the division.

Last but not least I thank my parents and girlfriend for their love and support in my two years of master study.

Contents

List of abbreviations

AC Alternating Current

ADC Analog-to-Digital Converter

CCD Charge Coupled Device

CMOS Complementary Metal Oxide Semiconductor

DC Direct Current

FWHM Full Width at Half Maximum

ICCD Intensified Charge Coupled Device

MCP Micro-Channel Plate

NEA Negative Electron Affinity

PEA Positive Electron Affinity

PMT Photomultiplier Tube

SEE Secondary Electron Emission

SEM Scanning Electron Microscopy

TE Thermionic Emission

1 Introduction

1.1 Motivation

Spark plugs are a component of major importance in spark-ignition(SI) engines. At the end of the compression stroke, high voltage is applied between the central and side electrode of a spark plug, and an electrical discharge, which refers to a process of gas ionization caused by an electrical field [1], is induced. The electrical discharge ignites the fuel-air mixture in the combustion chamber of the engine, starting the combustion process and enabling the engine to output power.

The formation of an electrical discharge introduces significant stress on the components involved. In a typical spark plug, prior to breakdown the peak voltage between two electrodes can rise to approximately 4-6 kV at an ambient pressure of 1 atm, and about 22 kV at 11 atm, which is a typical lower limit of pressure in an engine before ignition [2]. At medium or high load the pressure in the engine's combustion chamber can be even higher, making the breakdown voltage also higher. Maly [3] reported that the instantaneous current in a discharge can reach a maximum of a few hundred amperes. It was also reported by Maly that the gas temperature can reach a peak as high as 60000 K, and can stay stable at roughly 3000 K in the ending phase.

As a result of this harsh environment, the electrodes can be damaged during the duration of the discharge. The erosion of the electrodes will lead to deteriorating engine performance, in the form of misfires and finally a power down. Since the invention of spark plugs, various materials have been used in the manufacturing of spark plug electrodes, such as tungsten, nickel, platinum, and iridium [4], and new geometrical designs have been proposed in order to prolong the lifetime of spark plugs.

Despite all the efforts taken in developing long-lifetime spark plugs, current production still can't meet the requirements from the industry. The ignition system producer SEM AB reported a typical spark plug service interval of 45000 km in heavy-duty natural gas trucks, which is shorter than the lifetime of lubricant oil. As a result, extra downtime for the trucks is created because they must be stopped between necessary oil changing services to replace worn spark plugs. Lin, etc. [5] also reported that the typical service time of spark plugs is 1000 - 4000 hours, shorter than the desired time of 8000 hours by the industry. Furthermore, the current trend in the development of combustion in engines aims at creating leaner mixture and higher compression ratio due to efficiency and environment reasons. This requires larger breakdown voltage and higher energy sparks, which means the durability and reliability of spark plugs become a limitation on engine technology development. For these reasons, it is essential that the mechanism of electrode erosion be better understood, to help optimize the ignition system for a better spark plug lifetime.

1.2 Goal of the thesis

Previous studies [4–9] on the erosion of electrodes mainly focused on using scanning electron microscopy(SEM) and other imaging approaches to compare new electrode surfaces and damaged ones after a long time (100-600 hours) of service. The target of the presented work was to investigate the possibilities of having a diagnostic approach with significantly higher temporal resolution. Preferably it should be possible to investigate the degree of electrode wear during the duration of the spark discharge. One proposed technique is based on the use of a photomultiplier tube(PMT) for the detection of the emission intensity emitted by excited metal atoms ejected from the electrode. With the PMT the influence of different parameters of the spark discharge on the emission intensity, as well as the spark-to-spark variations of the intensity under a certain condition was studied. Additionally, spectrally filtered high-speed imaging will be used to acquire spatial information of such emission. Using these approaches the thesis aims at giving a preliminary understanding of temporal and spatial characteristics of electrical discharge emission, thus information on when, during the spark discharge, and where the main erosion of electrodes occurs.

2 Theory

2.1 Discharge modes

An electrical discharge can be divided into three phases which are breakdown, arc discharge and glow discharge phase. The following description of the three phases is mainly a summary of the information given in books by Maly [3] and Raizer [1] .

2.1.1 Breakdown

With the high voltage built up between the electrodes, the already existing free electrons and ions in the gas between the electrodes will be accelerated by the electric field. As the accelerated particles move towards the anode or the cathode, they will collide with other gas molecules. In a strong electric field the collision can lead to ionization of gas molecules, creating more electrons and ions. The newly ionized particles will also be accelerated by the electric field and more particles can be ionized. A sufficiently high electric field(50-100 kV/cm) can transfer enough kinetic energy to the charged particles that the rate of the generation of electrons exceeds that of the removal, which are mainly transport to the anode, diffusion to the walls and attachment to the positive ions in the gas, and start a so-called 'electron avalanche' process where the number of free electrons increases exponentially.

As electron avalanche is created by primary electrons which already exist in the gas prior to the high voltage, secondary electrons can be generated on the cathode which contributes to initiating more electron avalanches. The generation of secondary electrons can be achieved through secondary electron emission(SEE) where high energy ions hit the cathode and knock out electrons, and thermionic emission(TE) where the cathode surface gets heated up by plasma bombardment and emits electrons [10]. Secondary electrons can also be generated by UV light emitted by excited ions in the gas. Once enough secondary electrons are generated, the discharge becomes self-sustained, which corresponds to a breakdown. Criteria given in [1] indicates that the discharge becomes self-sustained when

$$\gamma[\exp(\alpha d) - 1] = 1, \alpha d = \ln(1/\gamma + 1); \tag{2.1}$$

where γ is the effective secondary emission coefficient for the cathode, α the Townsend coefficient for ionization, and d the distance between the electrodes.

In the breakdown phase, the voltage between the electrodes drops rapidly to about 100 V and a peak current of hundreds of amperes is reached. This process happens in a time range of nanoseconds. The breakdown happens in a very narrow channel of approximately 40 μm, which leads to a high electron density environment being built at the magnitude of 10^{19} e/cm^3. Such high electron density results in strong Coulomb force between the electrons and ions, and the interaction causes an efficient transfer of energy from the electrodes to the charged particles, thus a high level of ionization and a high gas temperature of up to 60000 K [3]. Fig.2.1 shows the trends of different parameters in the plasma generated by an electrical discharge.

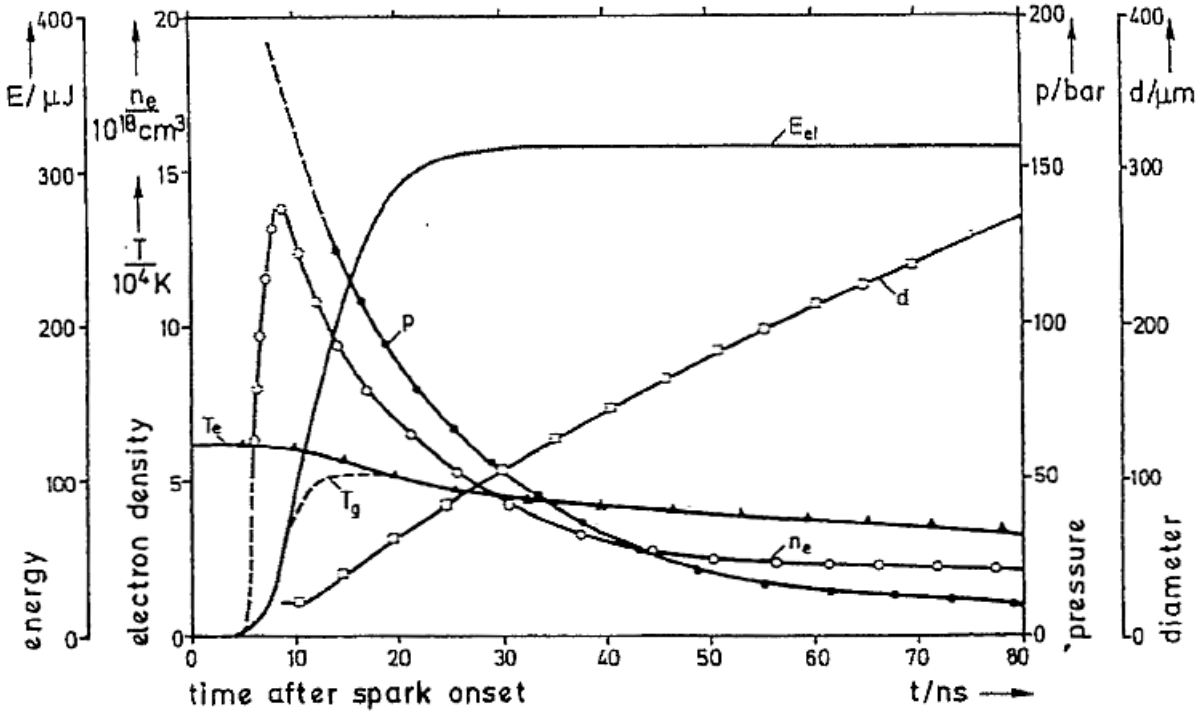

Figure 2.1: Plasma parameters of a breakdown in air at 300 K, 1 bar and 1 mm spark gap. E_{el}, electrical energy supplied to the electrodes; T_e, electron temperature; T_g, gas temperature; n_e, electron density; p, overpressure in the plasma channel; d, the diameter of the plasma channel [3].

The temperature rise is sufficiently rapid and the lifetime of the breakdown is so short that during and shortly after the breakdown the cathode would remain cold. However, the current in the plasma will eventually lead to a heated spot on the cathode surface, where thermionic emission is emitted. This marks the transition from the breakdown phase to the arc phase.

2.1.2 Arc discharge

The main characteristic of the arc phase is a relatively low potential difference between the plasma channel and the cathode, referred to as the cathode fall, which is about 15 V in an electrode gap of 1 mm, surrounded by air at 1 bar pressure. The arc can be sustained at such low cathode fall because the hot spots on the cathode surface can give sufficiently high thermionic field emission, forming an electron current nearly equal to the current in the plasma channel. For typical spark plug materials the temperature of the hot spots can reach their boiling points and substantial evaporation can happen, which leads to severe erosion of the electrode.

At the early stage of the arc phase multiple small and fast moving spots appear on the

cathode, whose diameters are typically $10^{-4} \sim 10^{-2}$ cm and velocities $10^3 \sim 10^4$ cm/s. Only negligible erosion happens at this stage due to presumably the small-scale explosions of the liquid metal. In about 10^{-4} s the small spots would merge into larger spots whose velocities are 2 orders of magnitude lower than the smaller spots'. In these larger spots, however, erosion due to thermal reasons becomes dominating and the erosion becomes more intense. These hot spots are reported to be able to act as sources of vapor jets, ejecting vapor at velocities of $10^5 \sim 10^6$ cm/s.

2.1.3 Glow discharge

A glow discharge is similar to an arc discharge. The major difference between glow discharges and arc discharges is that the cathode is cold in glow discharges. In such discharges the dominating mechanism of charge carrier generation is ion bombardment, which is inefficient compared with thermionic field emission. Therefore, the current in a glow discharge is typically less than 100 mA, much smaller than that in an arc discharge. Also due to the inefficient charge carrier generation, cathode fall in glow discharges is larger than in arc discharges, typically being 100-400 V or even higher [3].

The cold cathodes in glow discharges lead to the lowest erosion rates among all three different discharge modes. Absence of hot spots on the cathode surface makes sputtering the ruling source of erosion. Despite the erosion rate being low, however, the long duration of a glow discharge makes the total erosion not negligible. Considering the power and energy release functions, breakdown mode has the highest power but releases the smallest amount of energy; the arc discharge has both parameters in between; the glow discharge has the lowest power but the long duration leads to the most energy released [1].

2.2 Models of electrode erosion in electrical discharges

In this section three different models of electrode erosion are briefly introduced, which are particle ejection, evaporation and sputtering.

2.2.1 Particle ejection

Gray and Pharney made an observation on electrode surfaces that were damaged by different kinds of discharges and proposed a model of erosion by particle ejection in [11]. The SEM images revealed multiple spherical structures, referred to as particles in the paper, on one electrode, and circular-shaped craters on the other. They also reported erosion of electrodes observed in the form of small spheres, whose diameters are approximately 1 μm, being transported from one electrode to the other. Fig.2.2 shows a schematic drawing of what Gray claimed to be the main mechanism of particle ejection.

As mentioned in section 2.1.2, when an arc is sustained between the electrodes, small spots of molten metal must be present on the cathode surface to provide the sufficient quantity of electrons. When the ion beam hits the molten pool of metal, a force is applied towards the electrode, and the molten metal gets pushed away to the edge of the crater, as

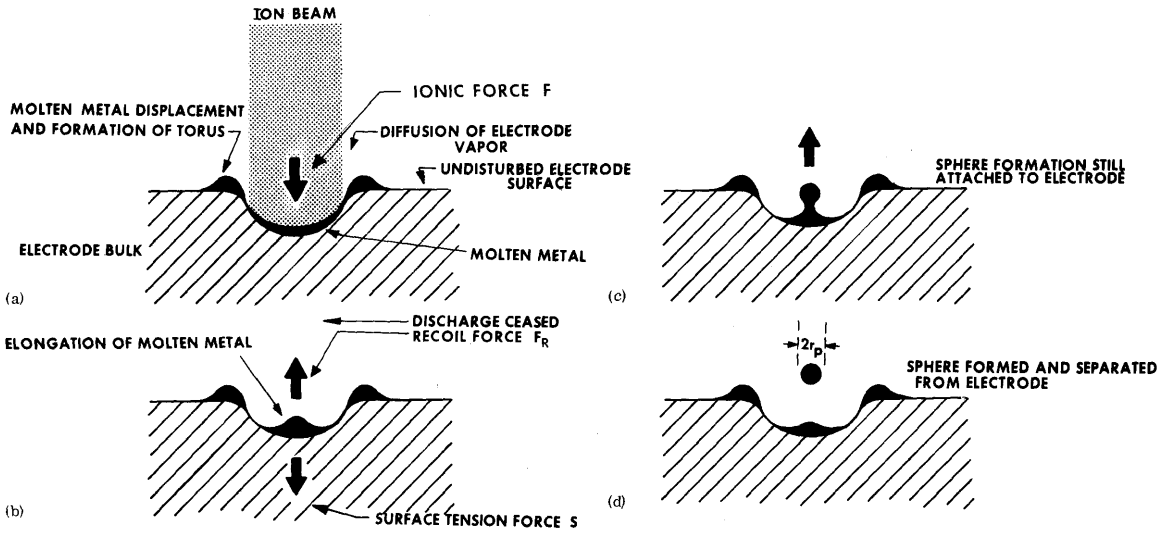

Figure 2.2: Schematic drawing of the particle ejection erosion model [11].

shown in fig.2.2(a). During this stage a recoil force is built on the liquid metal remaining in the crater to counter the ionic force F. When the discharge is terminated, the ion force dies out immediately but the recoil force remains. As shown in fig.2.2(b), the absence of the ion force results in the recoil force gathering material at the bottom of the crater. If the recoil force exceeds the surface tension force S that holds the metal together, the metal would form a sphere and be ejected from the crater.

The surface tension force S can be written as

$$S = 2\pi r_p \Gamma, \tag{2.2}$$

where r_p is the radius of the sphere that leaves the surface, as shown in fig.2.2(d), and Γ is the surface tension of the liquid metal. The ionic force F given by Augis, etc. [12] is

$$F = (I_+/e)(2m_i eV_s)^{1/2}, \tag{2.3}$$

where I_+ is the ionic current, m_i the ion mass in the beam, V_s the cathode sheath voltage, i.e. the cathode fall, and e the electron charge. The recoil force F_r is expected to be equal to or slightly weaker than F. As the criteria required for a sphere to be ejected is $F_r > S$, F should be reasonably stronger than S.

In [11], Gray and Pharney calculated the surface tension force S and the ionic force F in gold electrodes. S was estimated to be 0.047 dyn, with values of $r_p = 0.1$ μm, which is the average radius for gold particles, and $\Gamma = 750$ dyn/cm for gold at melting point. To calculate the ionic force F, mass of gold atoms $m_i = 197$ u, and $eV_s = 10$ eV in gold electrodes were taken. Base on the relationship between the ionic current and the electron current that $I_+/I \approx 0.1$, and the fact that $I = 0.5$ A in the case discussed, the ionic current can be estimated to be about 0.05 A. With a final assumption that ten current channels exist in the arc simultaneously, the ionic force was calculated to be about 3.2 dyn.

The calculation results showed that F was two orders of magnitude larger than S in gold electrodes. The difference between the two forces was sufficiently high that particles can be ejected even if F_r is one order of magnitude smaller than F.

2.2.2 Evaporation

In [13], a model was described by Coulombe and Meunier, stressing the important role of a high local metallic plasma pressure in a self-sustaining arc. In this model, a molten pool of cathode metal is described to be present on the cathode surface. Above the molten pool is a layer of metallic plasma, created by the evaporation of the cathode during the forming of the arc. In this metallic plasma, ionization of the vaporized metal atoms happens through collision, providing charged carriers that contribute to the sustaining of the plasma channel. Based on the model, the authors calculated that a minimum metallic pressure of 7-9 atm is required for a 10^9 A/m^{-2} current density on a copper cathode.

Based on this model, it can be deduced that evaporation of the cathode material contributes remarkably to the total erosion of the cathode. In [14], the same authors made calculation on the erosion rate of the cathode based on the same model. Their calculation yielded an erosion rate of 10-300 µg/C for copper cathodes, depending on the metallic vapor pressure. It was also mentioned in the paper that a higher pressure of the surrounding gas tends to reduce the erosion by evaporation, due to the fact that the metal vapor is confined in an area closer to the cathode surface.

2.2.3 Sputtering

Ref. [15] describes the electrode erosion mechanism of sputtering. As shown in fig.2.3, sputtering is a process including multiple collisions between atoms. Upon hit by high energy ions, atoms on the target material's surface gain kinetic energy from collision. The accelerated atoms can further collide with other atoms in the bulk of the target. If the energy of the incident ion is sufficiently high, there is a possibility that some atoms in the target get knocked out by other energized atoms. The direction in which the atoms leave the target can be random. In very thin films, sputtered atoms may leave the target in the same direction as the incident ions. In the erosion of electrodes, however, most sputtered atoms leave from the electrode surface, opposite from the incident direction of the plasma ions due to the bulkiness of the electrode. This is referred to as backsputtering. The atoms numbered 2 and 4 in fig.2.3 are examples of such backsputtered atoms. Various factors, such as the energy of the incident ions, the mass of the ions and the incident angle can affect the yield of the process.

2.3 Photomultiplier tubes and image intensifiers

2.3.1 Photomultiplier tubes

Based on [16–18], a simple description of PMTs is given in this section.

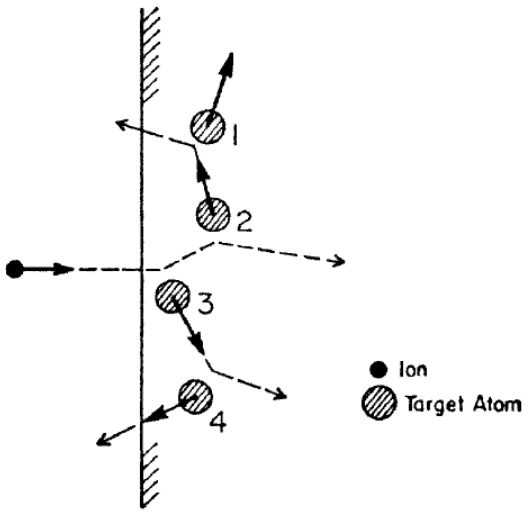

Figure 2.3: Schematic drawing of the sputtering erosion of electrodes [15].

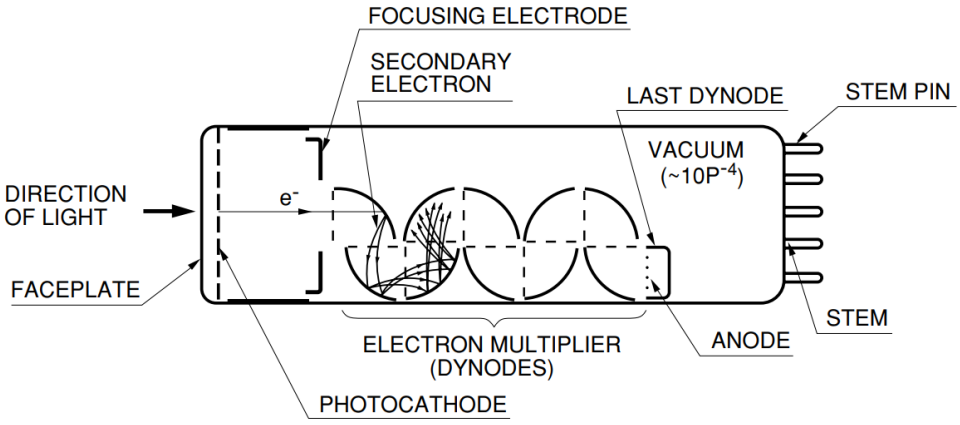

Figure 2.4: Schematic drawing of the structure of a PMT [16].

A photomultiplier tube is a vacuum tube capable of detecting very weak light signals. The detection can be divided into three stages: generation of photoelectrons upon incidence of light; acceleration and multiplication of secondary electrons; and finally the collection of secondary electrons and the readout of the signal. Fig.2.4 shows the basic structure of a PMT.

A photocathode is used in the generation of photoelectrons. Typically it is made of semiconductor materials. Solid state physics gives a description of the energy band structure of semiconductors: there exists a valence band that marks the energies that are allowed for electrons, a forbidden band within which the electrons are not allowed to exist, a vacuum barrier or vacuum level(E_{vac}) that marks the energy needed for an electron to be released into the vacuum, and an electron affinity(EA, written as η) which is the

energy difference between the conduction band maximum energy and the vacuum level, as shown in fig.2.5. Materials for photocathodes can be divided into two classes, namely positive electron affinity(PEA) whose conduction band minimum energy(E_{CBM}) is lower than E_{vac}, and negative electron affinity(NEA), whose E_{CBM} is higher than E_{vac}. Typical configurations are alkali photocathodes for PEA and III-V semiconductor photocathodes for NEA.

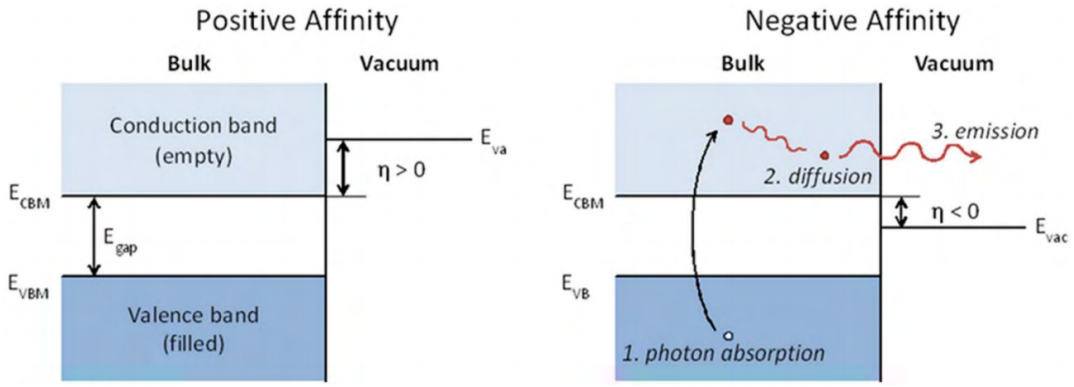

Figure 2.5: Basic energy band structure of positive affinity semiconductors(left) and negative affinity semiconductors(right). E_{CBM} is the conduction band minimum energy, E_{VBM} the valence band maximum energy, E_{vac} the vacuum level, E_{gap} the band gap defined as $E_{gap} = E_{CBM} - E_{VBM}$, and η the electron affinity defined as $\eta = E_{vac} - E_{CBM}$ [17].

When a photon with energy larger than the energy gap E_{gap}, defined as the energy difference between the conduction band minimum energy and the valence band maximum energy, is absorbed by a semiconductor material, an electron can be excited from the valence band to the conduction band. The excited electron can then diffuse in the bulk of the semiconductor, and, if the absorbed photon has enough energy to overcome the vacuum level, the electron can be emitted into the vacuum. This is called a three-step photoemission model. The minimum energy required for photoemission is $E_{gap} + \eta$ for PEA materials and E_{gap} for NEA materials. Therefore NEA materials can usually respond to longer wavelengths and have higher quantum efficiency.

Dynodes are responsible for the multiplication of secondary electrons in a PMT. They are often made from alkali antimonide, beryllium oxide(BeO), magnesium oxide(MgO), gallium phosphide(GaP), and gallium arsenide phosphide(GaAsP) coated on a metal substrate. When hit by a primary electron, a number of secondary electrons can be generated. The number of secondary electrons generated depends on the energy of the primary electron, and the function varies with different materials. In a PMT, a high voltage is applied between every two neighboring dynodes. The secondary electrons generated by one dynode gain energy from the electric field and act as primary electrons in the following dynode. Thus the number of electrons increases exponentially as they travel through the stages of dynodes.

The anode is the last stage of the detection. It collects the electrons generated in the

previous amplification stages and outputs a current signal to the outer circuit. Depending on the design of the PMT the anode can be in shape of a rod, plate or mesh. It is an essential condition that sufficient voltage difference is built up between the anode and the last dynode, to allow for an optimized electron collection.

2.3.2 Image intensifiers

The principle of an image intensifier is similar to that of a PMT, but with a few differences. Input photons are converted to photoelectrons on the photocathode; electrons are accelerated and the number of electrons is multiplied in the following stage, using a device called a micro-channel plate(MCP), comparing to the series of dynodes in a PMT; and finally the electrons hit a fluorescence screen, rather than an anode, to produce a stronger light signal that can be picked by the charge coupled device(CCD) or complementary metal oxide semiconductor(CMOS) afterwards. Using an image intensifier can also be beneficial in that it can reduce the exposure time, and that by choosing a proper fluorescent material UV sensitivity can be gained in a normal camera.

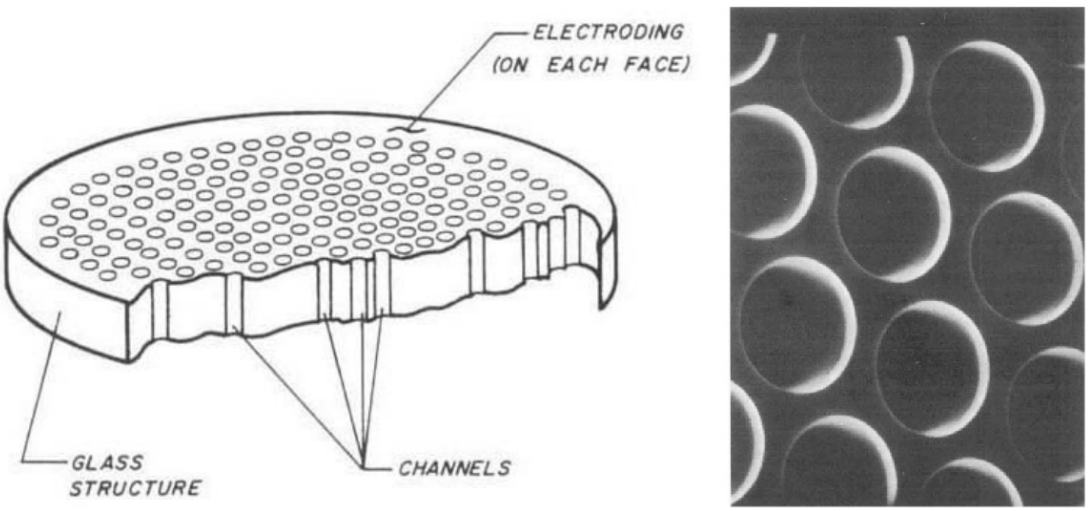

Figure 2.6: Schematic drawing of the structure of an MCP(left) [19]; scanning electron microscope image of MCP channels(right) [20].

The structure of an MCP is illustrated in fig.2.6. Typical MCPs have arrays of 10^4-10^7 micro-channels, each with a diameter of 10-100 μm and an aspect ratio(length to diameter ratio) of 40-100. The channels are arranged parallel, either orthogonal to the MCP input surface or with a bias of a small angle of about 8° [19]. The channels take about 55-65% of the plate area [20]. The spacing and dimension of the channels limit the spatial resolution of the intensifier.

In operation, a voltage is applied between the two faces of the plate. In this way, a potential gradient is built between the entrance and the exit to the channel. Incident electrons are thus accelerated by the electric field and are multiplied in number when they

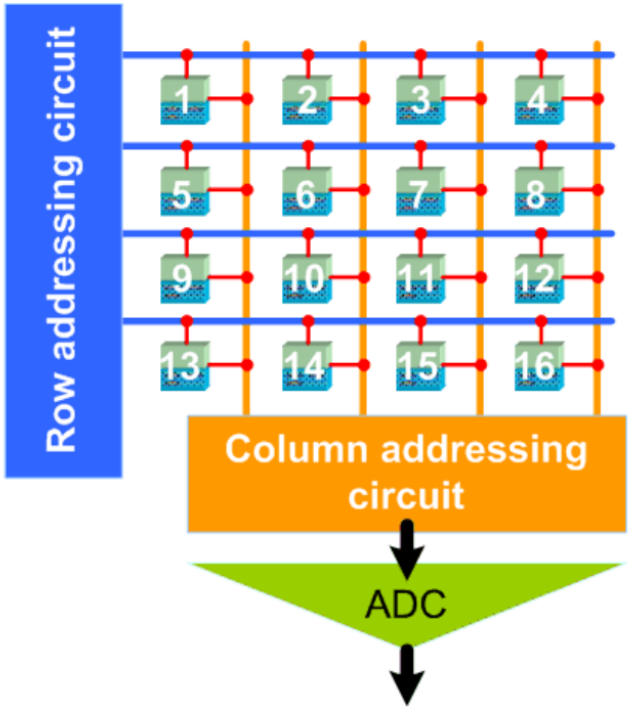

Figure 2.7: Layout of a pixel-by-pixel readout architecture CMOS detector [21].

hit the inner surface of the channel, similar to the multiplication process on a dynode surface.

2.4 High-Speed CMOS

CMOS technology is nowadays commonly used in building 2-D light detectors. A simple layout of a CMOS detector is shown in fig.2.7. Each pixel in a CMOS detector is a photodiode implemented with an amplifier. When receiving a light signal, the photodiodes generate charges, which get converted to voltage signals by each pixel's own amplifier. The signal can then be read out by the row and column addressing circuits directly. [22]. In the layout shown in fig.2.7, a so-called pixel-by-pixel readout structure is used, where one analog-to-digital converter(ADC) converts all voltage information in the pixels into digital output.

The structure shown in fig.2.7 is simple but clearly limited in frame rate. In order to reach higher frame rates, measures can be taken both in the structure of the detector and in the operation. One possible way of increasing the frame rate is to increase the number of ADCs. By assigning one ADC to each column, a per-column ADC(PC-ADC) structure can be built. Further improvement can be made by giving one ADC to each pixel, forming a per-pixel ADC(PP-ADC) structure. [21] reported a frame rate of up to 100k fps in the PP-ADC structure and 10k fps in the PC-ADC. The frame rate can be further increased by removing the ADCs and output analog signals directly [21]. On the operation level, the

frame rate can be increased by reading out only a selected region on the whole detector, a so-called window mode scanning, or by skipping a certain number of pixels before reading out a pixel, which is called subsampling [22]. These operation modes increase the frame rate, at a cost of a reduced resolution.

3 Experimental instrument and setup

3.1 Spark plug erosion test rig

The test rig was designed and produced by SEM AB. A pair of electrically isolated platforms held two commercial spark plugs, whose ground electrodes were removed to expose the central electrodes, to form an electrode gap. The two platforms were mounted on a translation stage to allow for adjustment of the electrode gap distance. A rotational stage enabled the spark to be rotated around an axis parallel to the horizontal plane. When the rotational stage is set up-straight, the upper electrode was connected to a replaceable ignition coil, and the lower electrode was grounded to act as the ground electrode. In the following text, the two electrodes will be referred to as the upper and lower electrode, as introduced here. The electrodes used in the experiment are one NGK IFR5J iridium spark plug as the upper electrode, and one NGK BCP7ES nickel spark plug as the lower electrode. A nozzle was placed next to the spark gap which can be connected to gas sources and introduce a cross flow to the spark. Photos of the test rig are shown in 3.1.

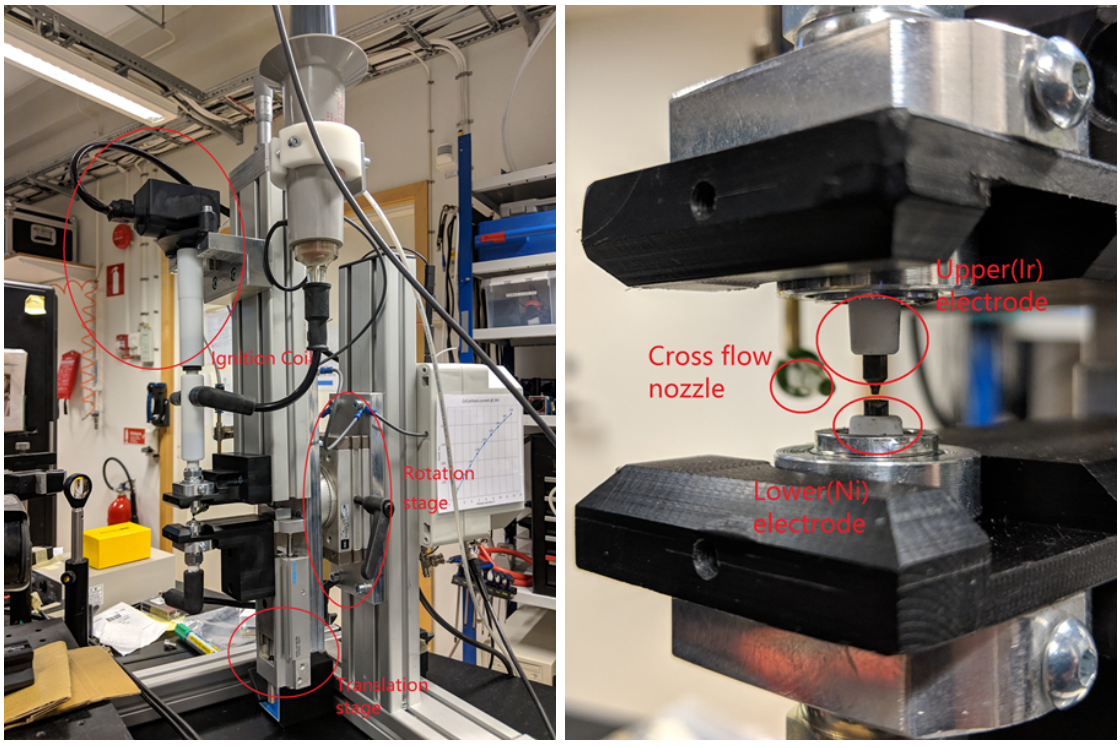

(a) (b)

Figure 3.1: Photo of the test rig (a) and a close-up photo of the electrodes (b).

Fig.3.2 shows a schematic diagram of the inductive ignition system used in the experiment. The discharge was controlled by pin 2. When driven high(over 2 V), the coil starts to charge; when driven low(below 1.2 V), the discharge is started. A pulse gener-

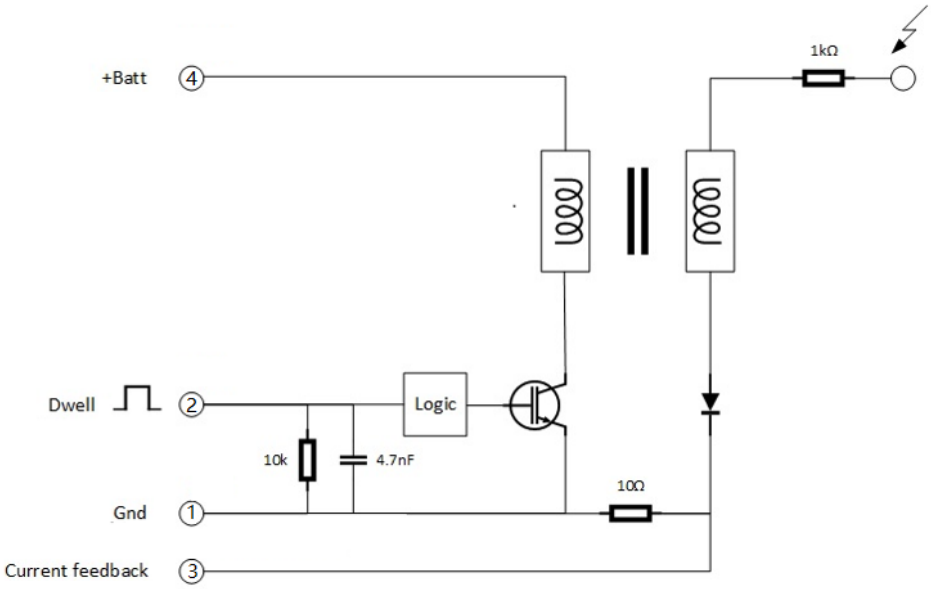

Figure 3.2: Schematic diagram of the inductive ignition system used in the test rig designed by SEM AB.

ator(Quantum composers 9514 Plus) was used in the experiment as the trigger source to the discharge and to other devices involved.

By changing the ignition coil, both inductive and capacitive sparks can be fired using the test rig. Through connecting the rig to a control module developed by SEM AB it is also possible to run both direct current(DC) and alternating current(AC) sparks. The module is also capable of creating multiple breakdowns in one spark, and when being run in DC mode, the bias on the upper electrode can be set on either positive or negative for each breakdown.

3.2 Spectroscopic measurements

A 300 mm Princeton Instruments Acton Spectrapro 2300i spectrometer was used for the spectroscopic measurements. The gratings used were 300 lines/mm and 1200 lines/mm. An intensified charge coupled device(ICCD) camera(Princeton Instruments PI-MAX II) was connected to the spectrometer to record the spectra. The emission from the spark was collected and focused onto the entrance slit by a B.Halle f = 100 mm f:2 UV achromatic lens. The spectrometer was calibrated with a mercury lamp. The mercury lamp emission data was taken from reference [23]. The spark gap was rotated 90 degrees along the rotational stage during the spectroscopic measurements, allowing for the spectrometer to resolve emission from either a plane near the upper iridium electrode or the lower nickel electrode. A schematic drawing of the setup used in the measurements is shown in fig.3.3. In the figure, black wires stand for triggers and blue for signals.

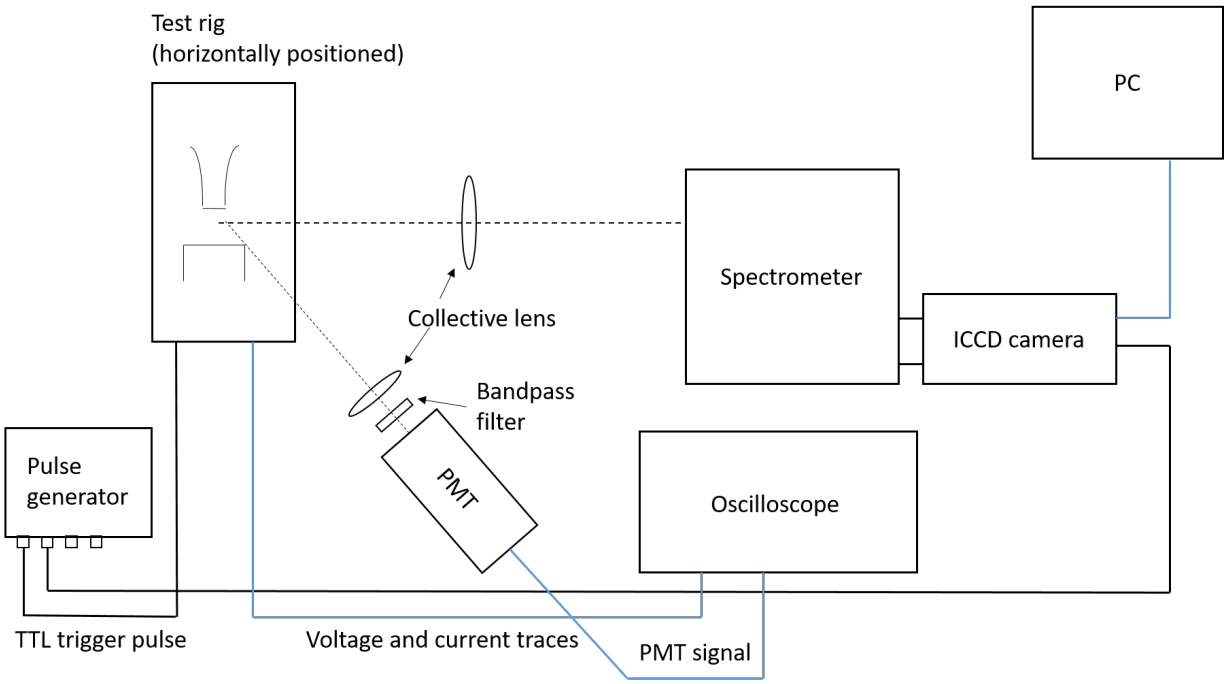

Figure 3.3: Schematic drawing of the experimental setup used in the spectroscopic measurements and the first set of PMT measurements.

3.3 Time-resolved PMT measurements

PMT measurements were carried out using a Hamamatsu h11526-20-nf photomultiplier tube controlled by a Hamamatsu c7169 power supply. Spectral filtering was achieved through an Edmund Optics 343 nm CWL, 12.5 mm Dia., Hard Coated OD 4 10 nm band-pass filter.

3.4 High-speed imaging

The high-speed imaging system consisted of an image intensifier(Lambert Instruments Hi-CATT intensifier), a high-speed CMOS camera(Photron Fastcam SA5), a UV lens(B. Halle 100 mm f:2 UV) and an extension ring(Nikon Bellows pb-6) for increased magnification. Two filters were used in the imaging: an interference filter(Edmund Optics 343 nm CWL, 50 mm Dia., Hard Coated OD 4 10 nm band-pass) and a high-reflector at 0 degrees that serves as a long-pass filter(CVI Lasers 355 nm 0° high reflector). A schematic drawing of the setup is shown in fig.3.4. All blue wires in the figure stand for trigger wires.

In the setup, an AND gate and an extra channel of the pulse generator were used to control the run time of the image intensifier. A schematic drawing of the pulses involved in the camera control is drawn in fig.3.5. The high-speed camera is constantly recording images when turned on. When the recording of a frame starts, a synchronization pulse is generated by the camera, and the pulse ends when the exposure of the frame ends.

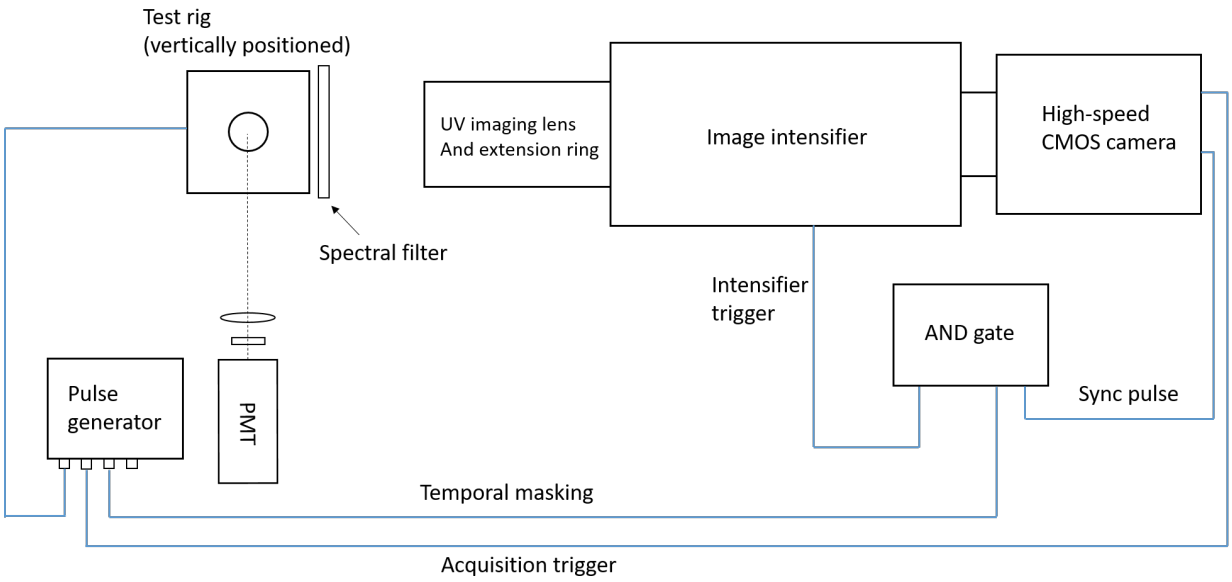

Figure 3.4: Schematic drawing of the setup used in the high-speed imaging measurements and the statistical PMT measurements.

Through the AND operation between the temporal masking and the synchronization pulse train generated by the camera, the trigger pulses to the image intensifier are confined to a desired period of time. When the image intensifier receives the output signal of the AND gate, it gets triggered for every rising edge in the pulse train. In the same time, the camera starts to save the recorded frames upon receiving of acquisition trigger's rising edge. Thus, by controlling the temporal position and width of the masking, the run time of the image intensifier gets controlled, and frames are saved during the desired time.

3.5 Self-built macro imaging system

Fig.3.6 shows a photo of the self-built imaging system. The imaging lens consisted of a Nikon cfi plan 10x/0.25 10.5mm WD microscope objective and a Nikon AF 80-200 mm 1:2.8 D zoom lens. The lens' focal length was fixed at 200 mm and focused on infinity to image the parallel light provided by the microscope objective. The camera used in the system was a Basler acA 1920-40gm CCD camera. The magnification of the system was 10:1 and the spatial resolution was measured to be 4.3 μm. In order to increase the strictly limited depth of field, the imaging system was mounted on a Thorlabs LTS300 motorized translation stage, and a control program was written in LabVIEW, enabling the system to automatically take pictures at different distances from the object.

A technique called focus stacking is used in the post-processing of the images. The basic principle of focus stacking is to identify all the in-focus areas in a series of photos with varying focal planes and combine them to form a photo with an extended depth of field. A free software CombieZP was used to carry out the focus stacking.

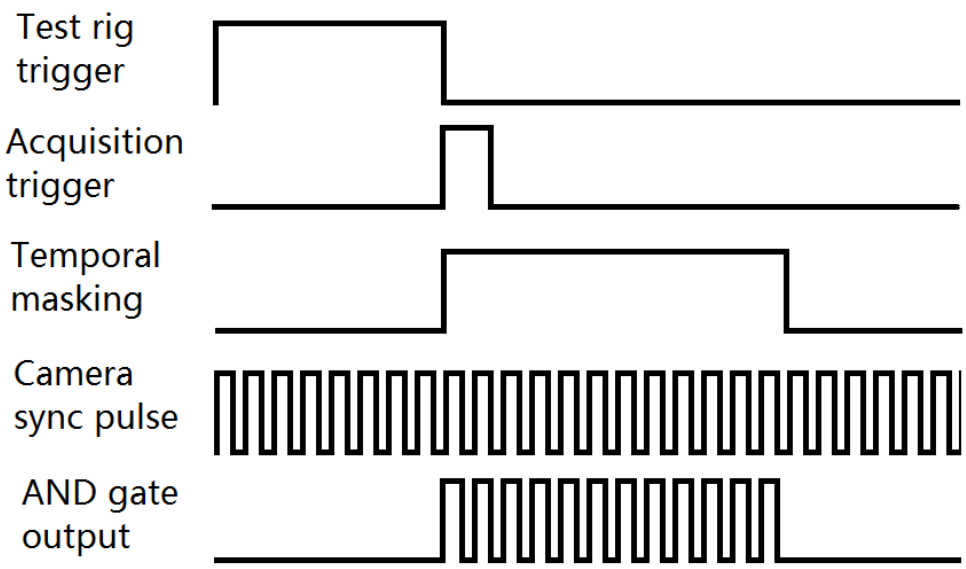

Figure 3.5: Schematic drawing of the pulse timing of the triggers.

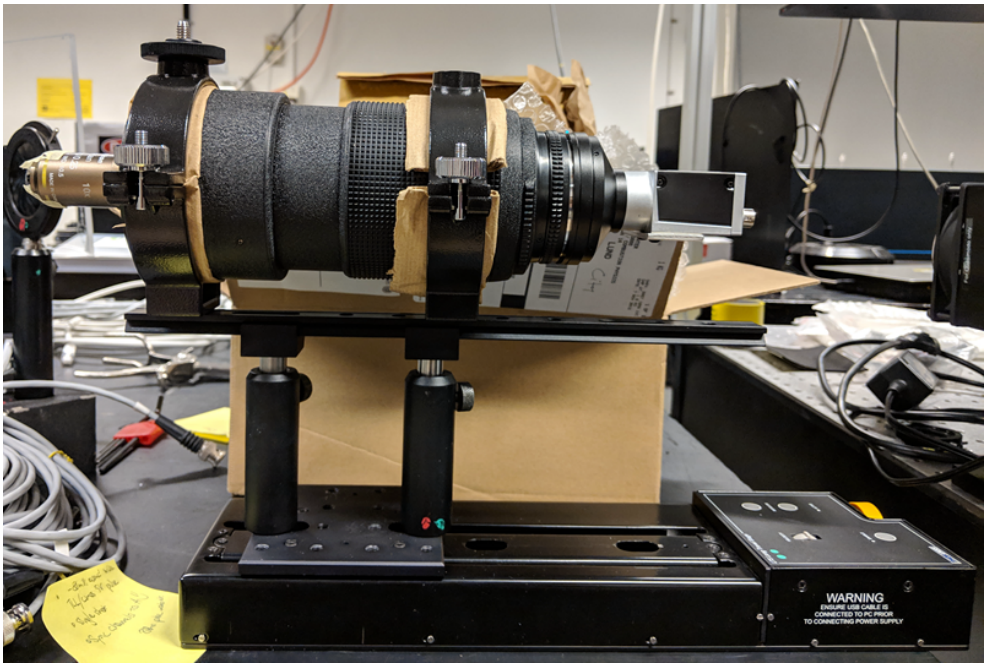

Figure 3.6: Photo of the self-built macro imaging system.

4 Experimental Results

4.1 Voltage and current profiles

During the spark discharge the secondary current(the current in the electrodes) and the voltage on the Ir electrode can be monitored using the oscilloscope. In figs.4.1 and 4.2 the current and voltage profiles of different spark modes measured in the experiment are demonstrated. In the modes shown in fig.4.1, the current readout channel was occupied for the generation of the special modes, making it not possible to measure the secondary current during the measurements. The profiles shown in fig.4.1 were provided by SEM AB afterwards. Note that the plateaus in the voltage curves are due to saturation of the channel. Actual voltage values exceeded the shown values and cannot be demonstrated. In each subfigure in fig.4.1, the voltage curve is shown in green and the current curve in blue. The scale of voltage is 500 V/div, with an offset of 970 V; the scale of current is 100 mA/div; and the time scale is 500 μs/div, with a -2 ms offset. The profiles in fig.4.2 were taken in real time while the spark was run by the inductive ignition coil.

Figures 4.1a and 4.1c to 4.1e are profiles of capacitive DC sparks. In fig.4.1a, at 0 μs a drop in both the voltage curve and the current curve marks the start of the discharge. Shortly after the build-up of the voltage, the breakdown begins. The values of voltage and current are negative because the upper electrode was negatively biased. Since no special modulation was done to the spark, the spark current gradually dropped after it peaked at the breakdown, at approximately 10 μs. The current became 0 at about 400 μs, indicating the end of the discharge. The spark duration can be determined from the current curve to be about 390 μs. The oscillation in voltage after the discharge ended was due to RC oscillation in the circuit.

In the 1 μF triple-breakdown DC sparks shown in figs. 4.1c to 4.1e, it can be observed that both a lower peak current and a shorter spark duration were reached in each breakdown event. The peak current is approximately 250 mA for the 2 μF spark, and 180 mA for the 1 μF spark. The spark duration for the latter is about 200 μs, compared to 390 μs for the former. Two consecutive breakdowns are triggered with an interval of 200 μs.

In the capacitive AC cases, as shown in figs. 4.1b, 4.1f and 4.1g, the initiation of the discharge is also at 0 μs, marked by the steep rise of the voltage and current. In the 2 μF cases figs. 4.1b and 4.1f, the instantaneous AC current peaked at about 250 mA. The first period of the LC ringing had the highest instantaneous current, and the current would decrease in the following periods. The period of the AC current can be observed to be about 140 μs and one discharge lasted for about 510 μs, the end of which is marked by the instantaneous current decreasing to zero, similar to the DC cases. In fig.4.1f the second spark was fired about 300 μs after the first spark.

Fig.4.1g shows a capacitive AC spark with a longer duration of approximately 1 ms. This is achieved by implanting five 1 μF capacitors into the ignition system. As can be observed in fig.4.1g, the whole spark duration can be divided into 2 stages, the first of which consists of five periods of AC current oscillating between +140 mA and -200 mA, and the second consists of five periods oscillating between +80 mA and -100 mA. This

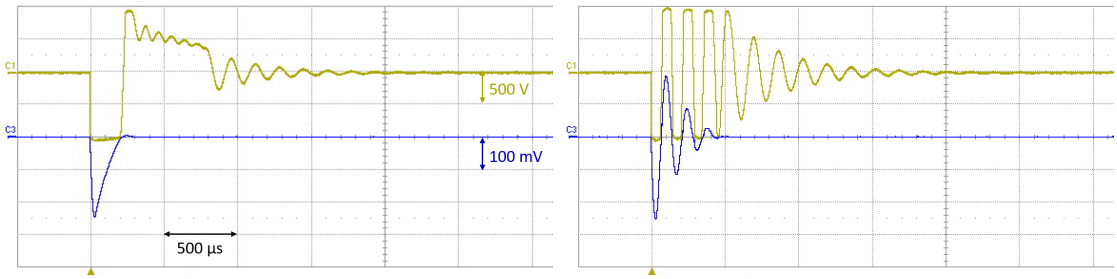

(a) 2 µF DC

(b) 2 µF AC

(c) 1 µF DC, triple-breakdown. positive bias

(d) 1 µF DC, triple-breakdown, negative bias

(e) 1 µF DC, triple-breakdown, negative-positive-negative bias

(f) 2 µF AC, double-breakdown

(g) 1 ms AC by 5 1 µF capacitors

(h) 100 mA, 1300 µs DC

Figure 4.1: Voltage and current profiles of sparks in different modes, recorded and provided by SEM AB. The green curves are the voltage at 500 V/div with 970 V offset, and the blue curve is the current at 100 mA/div. Time scale is 500 µs/div.

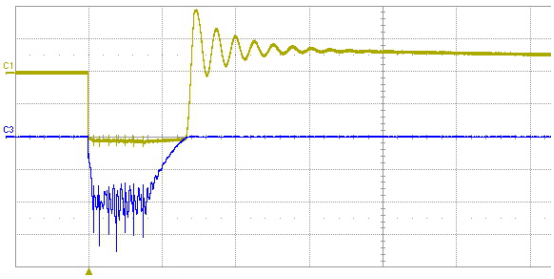

(i) 200 mA, 750 µs DC

Figure 4.1: (Continued) Voltage and current profiles of sparks in different modes, recorded and provided by SEM AB. The green curves are the voltage at 500 V/div with 970 V offset, and the blue curve is the current at 100 mA/div. Time scale is 500 µs/div.

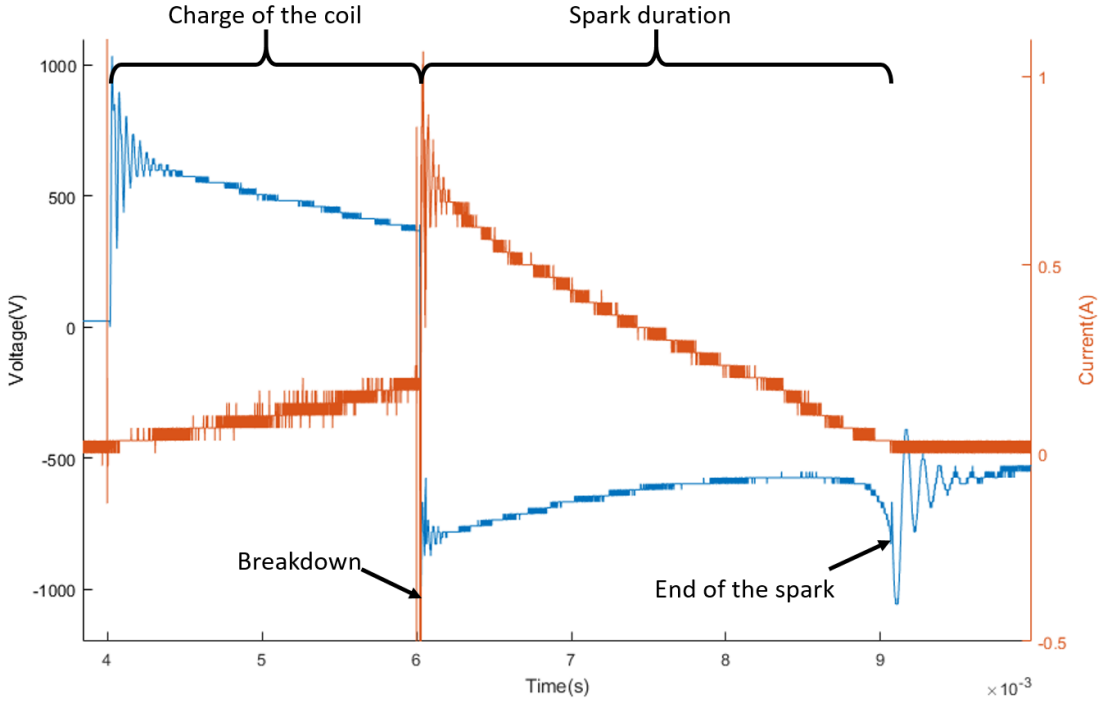

Figure 4.2: Current and voltage curves of an inductive spark with 2 ms charging time and 6.4 A primary current. The blue curve is the voltage and the orange is the current.

two-stage current profile was constructed by combining the first periods of the five 1 µF together and then the five second periods. By comparing the currents and periods of the 1 µF and 2 µF sparks, it can be observed that 2 µF sparks have longer periods and higher currents, similar to the DC cases.

Figures 4.1h and 4.1i are profiles of a special kind of sparks. Here modulation was applied to the spark, and as a result, compared to the decreasing currents as observed in

figs. 4.1a and 4.1c to 4.1e, the spark current was kept at a certain level for a desired amount of time. This mode can dispatch more energy into the spark, enhancing its ignitability.

Fig.4.2 shows a plot of an inductive DC spark's current and voltage curves recorded in the lab, whose dwell, i.e. the coil charging time, was 2 ms and the primary current was 6.4 A. Note that the current recorded in the figures is the secondary current.

As shown in fig.4.2, the first rise in voltage marks the start of the high input. After 2 ms, pin 2, shown in fig.3.2, was driven low, and the discharge began after a short delay of about 2 µs. The voltage readings are negative during the discharge because the Ir electrode whose voltage was measured was negatively biased. In the following context, the voltage will be referred to as absolute values. The voltage would first rise to tens of kilo-volts in a time of 5-10 µs, and drop to about 600 V in under 1 µs. The current can rise to above 10 A, as described in section 2.1.1. The current first went through a quick drop after the breakdown and then decreased slowly. The spark was considered ended when its current reached 0. As can be seen in fig.4.2 after the discharge ended the voltage curve began to oscillate. This phenomenon, according to Jakob Ängeby, the R&D manager of SEM AB, is due to LC oscillation in the circuit.

In this kind of sparks, the properties of the sparks are closely related to the trigger signal sent to pin 2. The longer the dwell, the longer the coil will be charged, and thus longer spark duration and higher primary current can be reached. At ambient pressure the spark voltage is affected by the spark gap distance. A larger spark gap results in both higher voltage at the breakdown and higher voltage during the discharge, and the spark duration is reduced. When introduced a cross flow, a decrease in spark duration can be observed.

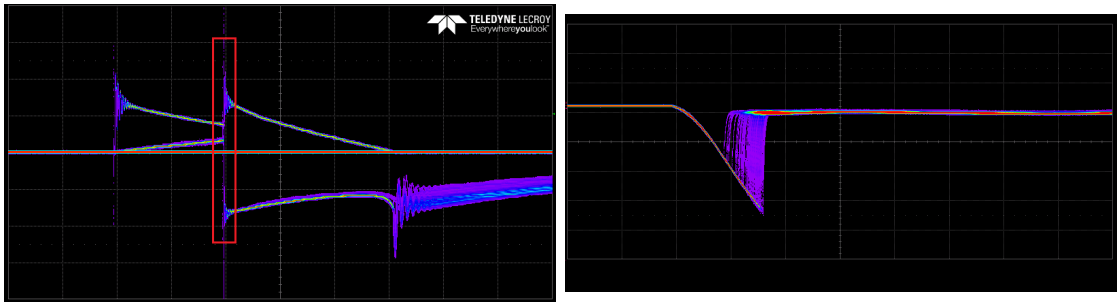

(a) (b)

Figure 4.3: Persistence test on 537 current and voltage curves (a) and persistence test on 500 breakdown voltage curves (b). In (a), the scale is 485 V/div for voltage, 440 mA/div for current, and 1 ms/div for time. (b) shows zoomed-in curves for the breakdown, which correspond to the area marked by the red rectangle in (a), and the scale is 5.1 kV/div for voltage and 5 µs/div for time.

Persistence tests were done on the inductive ignition coil, and some results are shown in fig.4.3. In fig.4.3a, 537 current and voltage curves were recorded and drawn, with the sparks run without cross flows. As can be seen, both the current and the voltage curves

show little spark-to-spark variation during the charging phase. During the spark, however, as the current curves still show good persistence, some variation in voltage can be observed. Some sparks tend to have a lower voltage than the majority. Furthermore, voltage variation becomes larger after the spark ends. In the oscillating tail of voltage curves, the persistence can be observed to be very poor.

In fig.4.3b, 500 new voltage curves during breakdown were recorded. The curves were recorded at a time scale of 5 µs/div and a voltage scale of 5.1 kV/div. The area shown in fig.4.3b corresponds to the area marked by the red rectangle in fig.4.3a. It can be observed that the breakdown voltage varied in a wide range, between about 10 kV and 17 kV. It is also shown in the figure that the voltage across the spark gap was built up almost linearly in time. The voltage build-up time ranges from about 5 µs to 8 µs.

4.2 Spectroscopic measurements

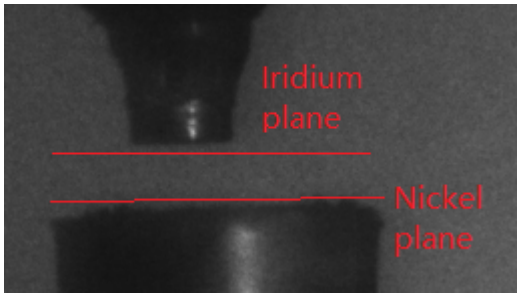

Figure 4.4: Photo of the electrode gap taken with the high-speed camera.

In fig,4.4, a photo of the two electrodes taken with the high-speed camera is shown. The electrode with a smaller diameter is the iridium electrode, and the other is the nickel electrode. The two planes where emission spectra were taken were marked by red lines in the figure, as described in section 3.2. In fig.4.5, the x-axes indicate the wavelength, and the y-axes correspond to points across the surfaces of the electrodes.

500 spectra of different sparks were recorded on each plane, and four were chosen to be shown here in fig.4.5 to demonstrate the results. The sparks measured in this section were fired using an inductive ignition coil, with 2 ms dwell and no cross flow, and the upper electrode was negatively biased. The current and voltage profiles of this running condition were the same as fig.4.2. Figures 4.5a to 4.5c were taken on the nickel plane, and fig.4.5d was taken on the iridium plane, as marked in fig.4.4. Two 1-D spectra, shown in fig.4.6a and fig.4.6b, were acquired by adding up all values on each column of fig.4.5b and fig.4.5c respectively. All spectra were recorded with a 1200 lines/mm grating centered at 350 nm, and the exposure time was 3 ms.

In fig.4.6a, three emission bands locating at 337.0 nm, 353.6 nm and 357.6 nm can be observed. These bands can be identified respectively as the N_2 C-B (0,0), (1,2) and (0,1) bands. In fig.4.6b, sharp atomic lines can be seen on top of the three nitrogen emission bands. By comparing the measured wavelengths with data found in [24], the lines between

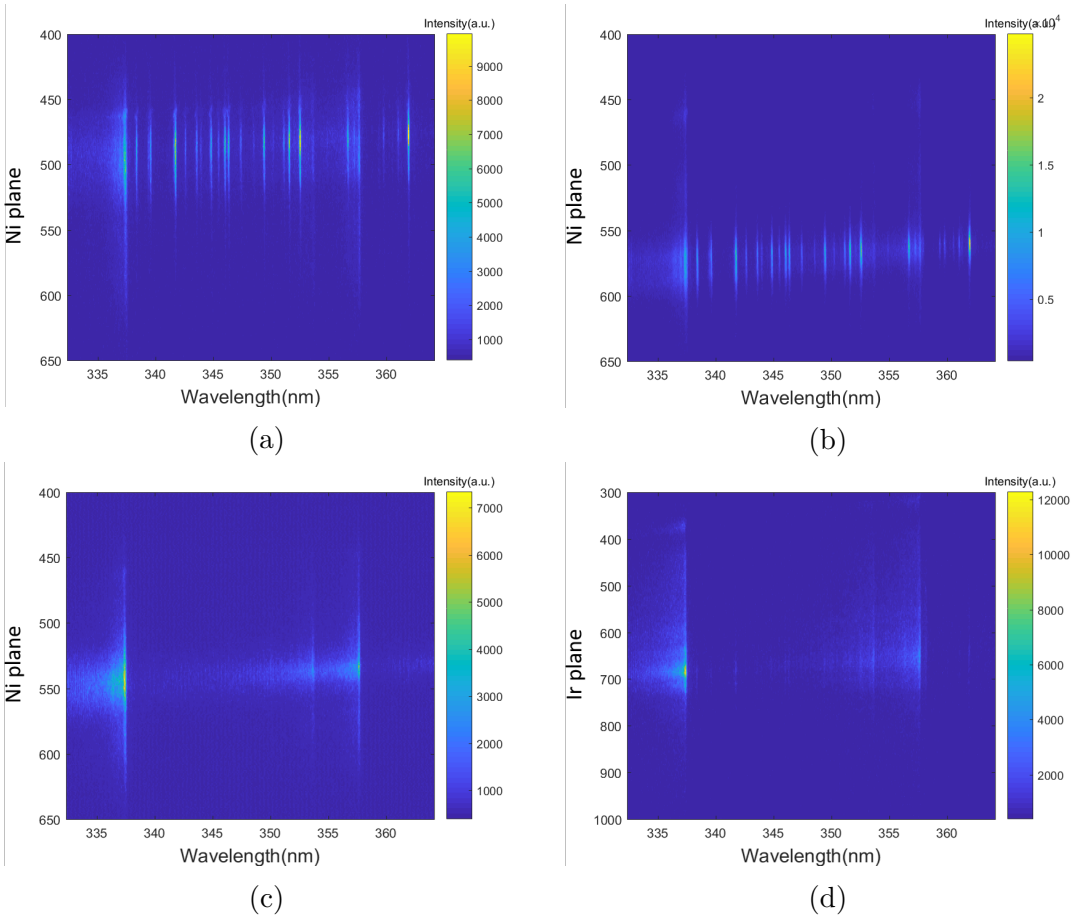

Figure 4.5: Emission spectra of the spark. (a), (b), and (c) were taken near the lower electrode, and (d) was taken near the upper electrode.

N_2 (0,0) and (0,1) bands were found to be Ni I lines, the source of which is vaporized metal atoms coming from the nickel electrode. Measured spectral data and the reference data are listed in table 4.1. For convenience purposes, the measured intensity of the 341.4 nm peak was set to 1000, and the intensity of other peaks was normalized accordingly. Similar measurements were done by Kim, etc. in [25], and the same observation of nitrogen bands and nickel atomic lines was reported in this spectral range.

By comparing the spectra of the Ni plane with those on the Ir plane, it can be observed that nickel atomic emission only appears near the nickel electrode. This indicates that the excitation of nickel only happens near the lower electrode surface. Based on this observation, conclusion can be drawn that vaporized nickel atoms can hardly travel to the other electrode. If any, no excitation of the atoms can be recorded. A further comparison was made between the two cases by adding up all 500 spectra together. As shown in fig.4.7, only very weak peak, almost unresolvable, can be observed at 338.0 nm, 339.2 nm and 341.4 nm in the summed spectrum on the Ir plane. In contrast, most lines listed in table 4.1 can be observed in the summed spectrum of the Ni plane. This further proves

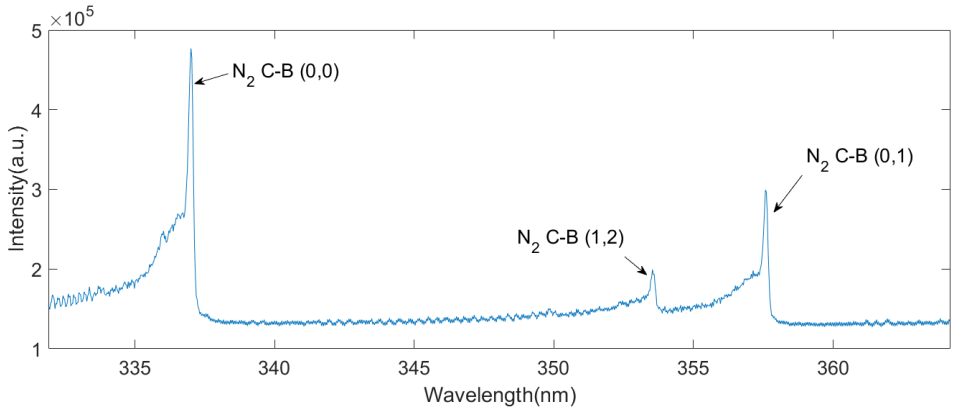

(a)

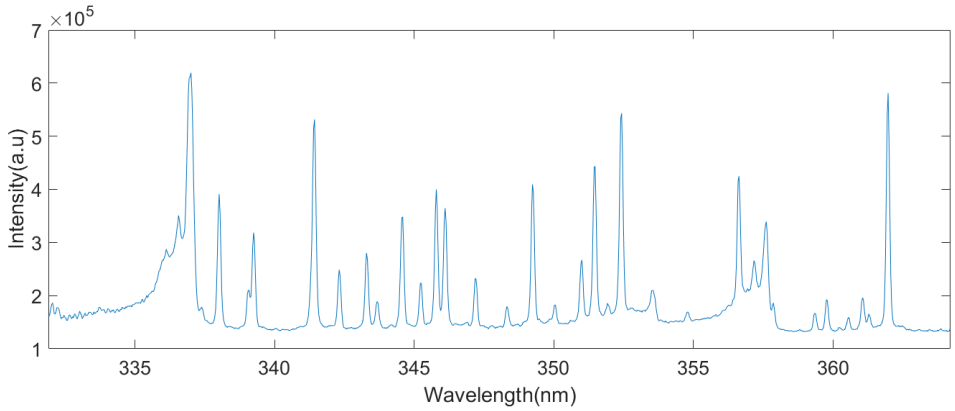

(b)

Figure 4.6: Spectra calculated from fig.4.5c(a) and fig.4.5b(b).

that strong atomic lines, i.e. the excitation of nickel atoms in the gas phase can only be observed near the nickel electrode. In section 2.2.2, spark erosion through evaporation was briefly introduced. The nickel emission intensity can be used to illustrate the degree of evaporation for the nickel electrode, and thus the rate of erosion of the nickel electrode. Higher intensity of nickel emission corresponds to a larger number of excited nickel atoms in the gas phase, as a result of higher erosion of the electrode.

By comparing figs. 4.5a and 4.5b with fig.4.5c, it can be seen that nickel lines didn't appear in all sparks measured. To further study this phenomenon, the intensity of the 341.4 nm peak was chosen as an indicator of total nickel emission intensity, and a histogram plot with 50 bins was made from the 500 hundred spectra recorded in the plane near the Ni electrode, which is shown in fig.4.8. An obvious spark-to-spark variation in the emission intensity can be seen in the figure. The background signal intensity in spectra of single sparks can be estimated in figs.4.6 to be about 1.4 $\times 10^5$ counts. In fig.4.8, 117 out of 500 spectra showed weak signal intensity similar to the background level at 341.4 nm. This low intensity indicates little to no nickel emission recorded. Fig.4.5c is an example of such spectra. In spectra where an emission intensity of over 1.4 $\times 10^5$ counts was recorded,

Table 4.1: Wavelength and intensity of the peaks measured in the experiment and corresponding data from the NIST handbook [24]

Measured wavelength(nm)	Measured relative intensity(a.u.)	Wavelength in NIST Handbook(nm)	Intensity in NIST Handbook(a.u.)
338.0141	740	338.057	400
339.0569	400	339.1043	150
339.2465	600	339.2986	400
341.4269	1000	341.4764	1000
342.3117	470	342.3708	200
343.2913	530	343.3556	300
343.6705	360	343.7278	120
344.5869	660	344.6259	600
345.2189	420	345.2889	150
345.7877	750	345.846	600
346.1037	690	346.1652	600
347.1781	440	347.2545	200
348.3157	340	348.3777	70
349.2321	770	349.2956	700
350.0221	340	350.0851	80
351.0017	500	351.0335	300
351.4441	830	351.5052	800
351.9181	350	351.9765	80
352.4237	1000	352.4536	1000
354.7937	320	354.8182	40
356.6265	800	356.6372	600
357.1637	500	357.1864	120

the corresponding events can be considered to have nickel emissions. Among the nickel-appearing events the intensity can still vary widely. In a total of 383 events with nickel emission, 189 events had a signal intensity of below 1.82 $\times 10^5$ counts. This means that about 50% of the events with gas phase nickel only gave very low emission. The number of events drops quickly as the intensity increase. In rare cases (7 out of 500), the peak intensity can reach higher than 9 $\times 10^5$ counts, about 4 times the intensity of the weakest ones. The event with the highest signal intensity at 341.4 nm reached 1.1 $\times 10^6$ counts.

Restricted by the max acquisition rate of 10 Hz of the camera, it is not possible to do high-speed spectroscopic measurements with the setup. However, it is desirable to study the temporal development of the nickel emission intensity. One possible way of gaining temporal resolution is to use a PMT. To do this a filter must be used to filter out a spectral region whose intensity can be representative of the nickel emission intensity. A 10 nm region centered around 343 nm was chosen, and the intensities of all channels in the region were added for each spectrum. The resulting histogram with 50 bins is shown in

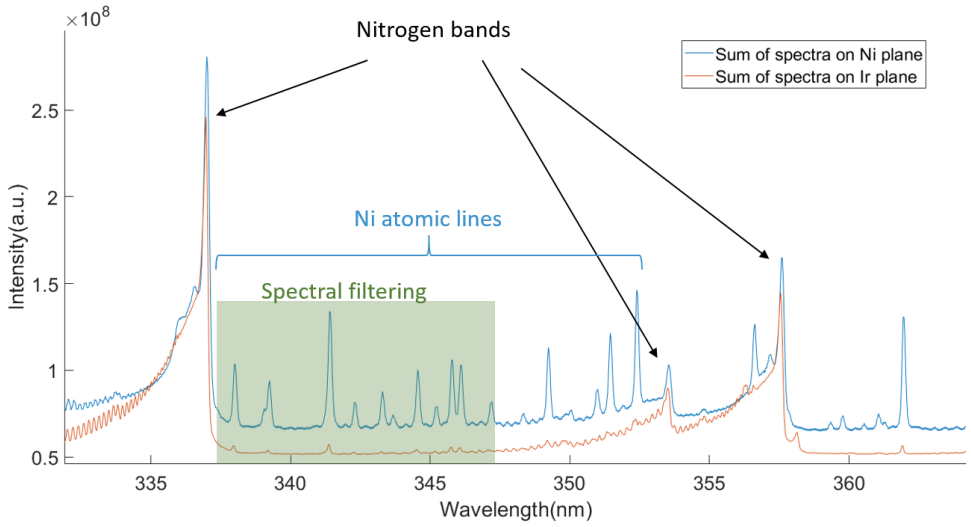

Figure 4.7: Sum of all spectra recorded on the Ni plane(blue) and the Ir plane(orange).

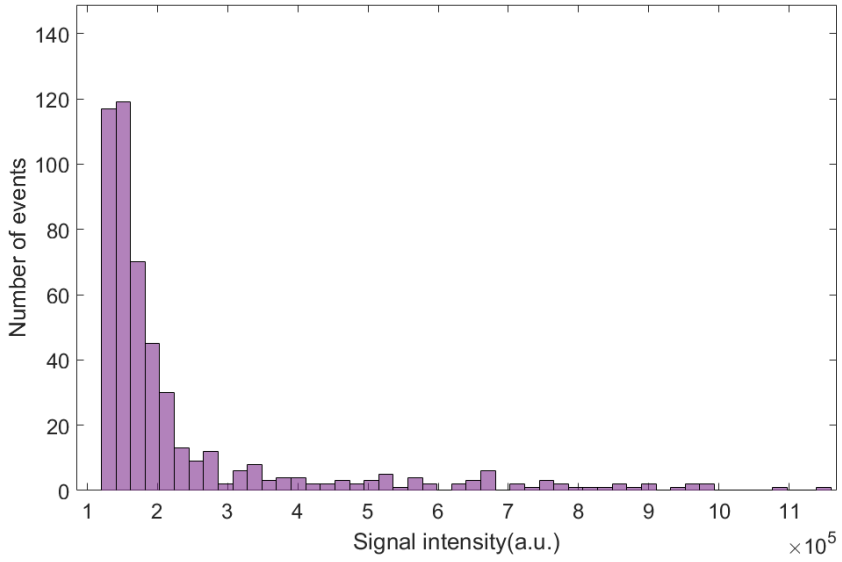

Figure 4.8: Histogram of the intensity of the 341.4 nm peaks.

fig.4.9.

Comparing fig.4.9 with fig.4.8, it can be seen that the distribution towards the higher intensities is similar in the two figures. Minor difference can be seen in the low-intensity region, especially the first two bins. A major drawback of using the total intensity of the 10 nm wide window is that it is not trivial to find a threshold separating the events with nickel emission with the ones without. However, serving as a qualitative method of observing the nickel emission intensity, the window is representative.

Spark-to-spark variation can also be seen in spatial positions. As is shown in figs. 4.5a

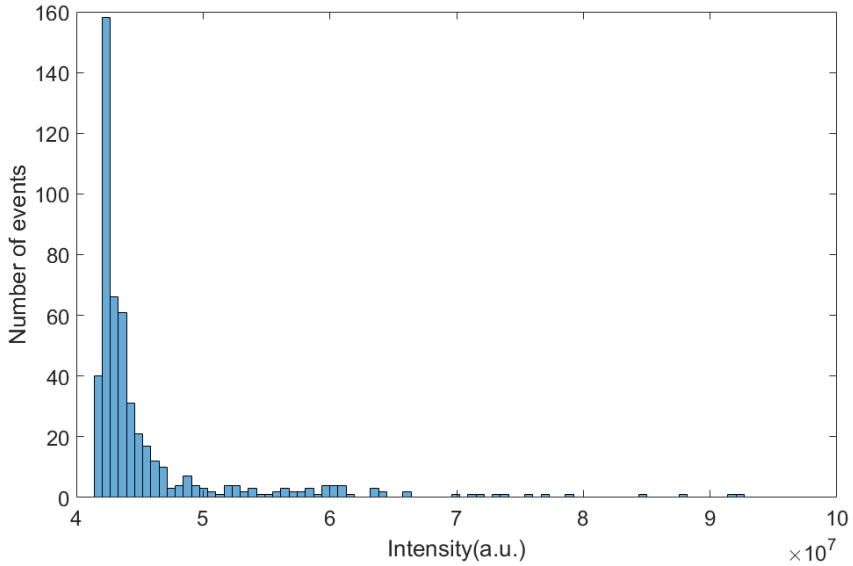

Figure 4.9: Histogram of the total intensity in a 10 nm spectral range, centered at 343 nm.

and 4.5b, the intensity peak appeared at different locations along the y-axis. This indicates that in different sparks the plasma channel can hit different spots on the nickel surface. This effect will be further studied in the high-speed imaging section.

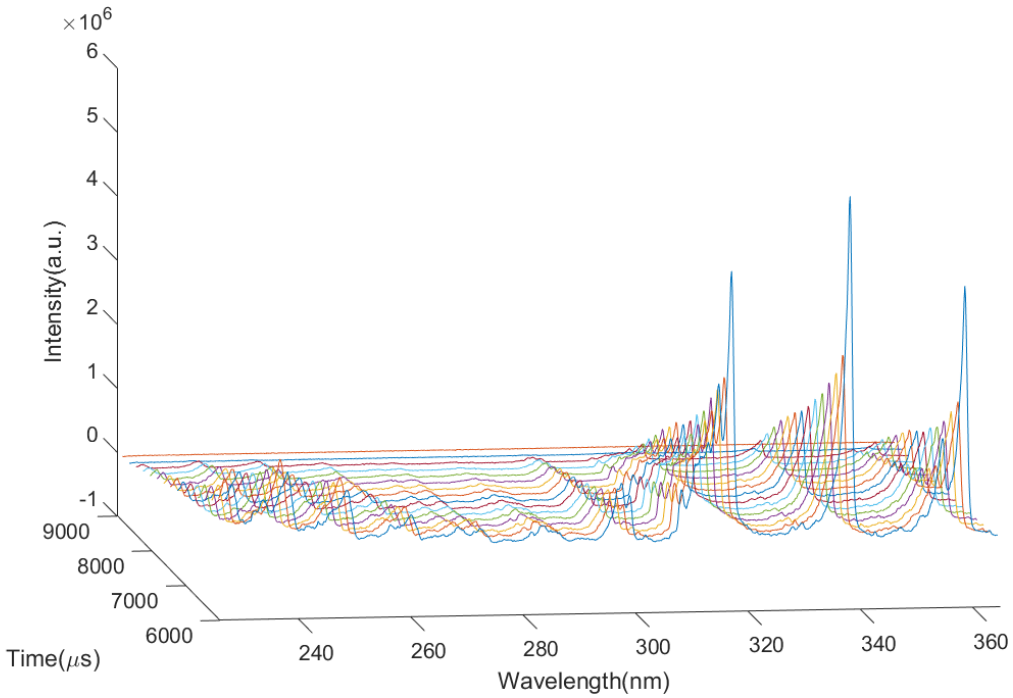

Figure 4.10: Spectra sequence recorded at different delay with respect to the breakdown.

In the spectra, it can also be observed that the intensity of the nitrogen peaks is relatively stable. Therefore it is possible to study the intensity variation of those peaks as a function of time during the discharge, by recording spectra of different sparks at different delay time relative to the breakdown. In fig.4.10, a sequence of such spectra is shown. The spectra were taken with a 300 lines/mm grating centered at 300 nm. The acquisition of the first spectrum was started when breakdown happened. Each spectrum following was recorded with a delay of 200 μs with respect to its previous one, and the acquisition time for all spectra was 100 μs.

As shown by the spectra, the intensity of the nitrogen bands reached the maximum right after the breakdown. In the following 200 μs, the intensity almost dropped by 50%. The decrease in intensity continued as the delay was increased. The intensity of the nitrogen bands can be seen as a near-exponential function of time after breakdown. Similar analysis cannot be used in nickel peaks due to their randomness.

4.3 PMT measurements

Based on the spectroscopic measurements, it was found that the emission intensities between 338 nm and 358 nm can serve as a good marker of evaporation erosion of the nickel electrode. Inspired by this conclusion, a band-pass filter centered at 343 nm, with a full width at half maximum(FWHM) of 10 nm, was chosen to filter out a region of interest, and the intensity variation of this region was further studied using a PMT. The time-resolved PMT measurement results are shown in section 4.3.1. Also, noticing the remarkable spark-to-spark variation in the properties of the sparks, statistical approaches were used in the PMT studies, and the results are shown in section 4.3.2. Note that the PMT signal values are negative in the figures but are referred to as absolute values when referred to.

4.3.1 Time-resolved PMT measurements

In fig.4.11, a PMT signal curve is shown in orange. The blue line is the corresponding voltage trace of the spark, shown here as an indication of what phase the spark is in. From the voltage curve it can be told that the charging of the coil started at 4 ms and lasted for 2 ms. The breakdown happened at about 6 ms, marking the start of the spark. It ended at about 9 ms, having a spark duration of about 3 ms.

Due to strong electrical noise introduced by the breakdown, the PMT reading at the breakdown cannot be trusted. The data is only reliable after the breakdown. It can be seen that in this case, the emission intensity of the filtered spectral range started to increase after the breakdown, and reached a peak at about 0.4 ms after breakdown. The intensity began to drop afterwards, but a slight rise of the signal can be observed at about 1.3 ms after breakdown. The decrease in intensity continued after the small peak and dropped to near 0 at about 2 ms after breakdown. In the next 1 ms, the weak intensity decreased very slowly and finally reached 0, about the same time when the spark ended, as suggested by the voltage profile.

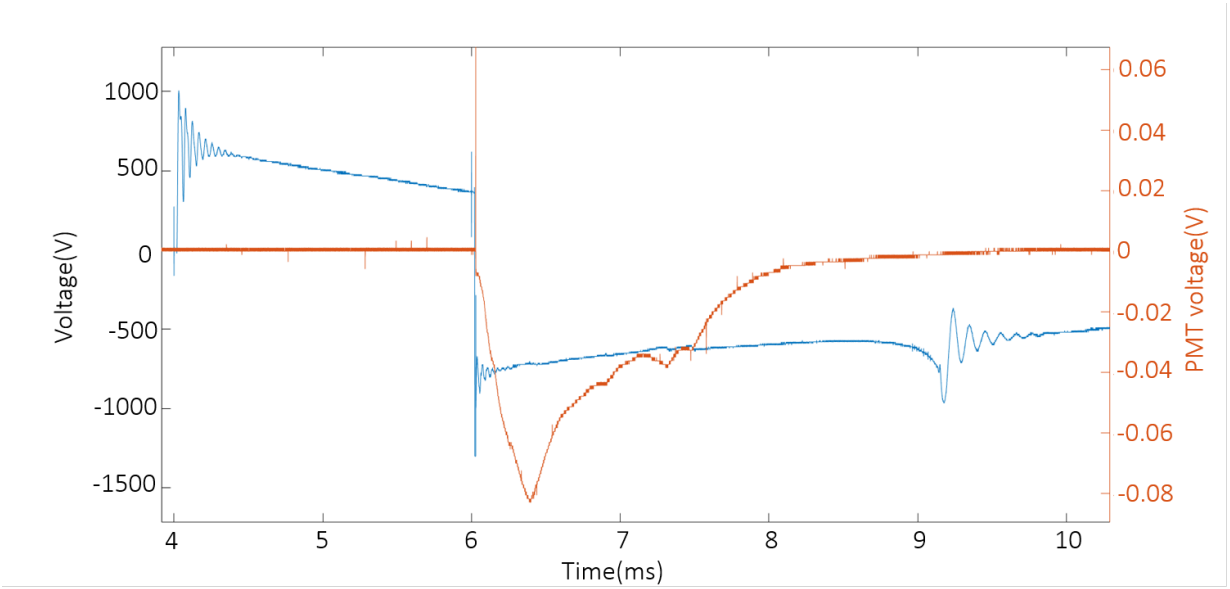

Figure 4.11: Spectrally filtered PMT signal and voltage of the spark.

This behavior of the 343 nm spectral range is clearly different from the nitrogen peaks, whose intensity peaked right at the breakdown and constantly decreased in the following phase of the spark. The PMT signal suggested that the evaporation of the electrode requires some time(about 0.5 ms in this case) to reach the maximum, and the number of Ni atoms in the gas phase decreases afterwards. The time when the PMT signal reached the maximum is when the erosion of the electrode is the most intense.

In fig.4.12, multiple records of PMT signals were shown, one of which is the weakest recorded in the whole data set(the red curve, marked as background) serving as a baseline of the signal intensity, and the others being the ones with relatively high peak intensities, indicating the existence of nickel emission in the sparks. More events with high peak intensities were recorded but excluded from the figure due to readability reasons. The data set was recorded with 2 ms dwell. A nitrogen cross flow was introduced to maximize the possible difference between different sparks.

A clear difference can be seen in the recordings. The strongest signal was recorded in event no.4, drawn in a purple line in fig.4.12. It peaked at about 0.75 ms after breakdown, with an amplitude of approximately 0.095 V. In contrast, the background intensity peaked at about 0.5 ms after breakdown with an amplitude of about 0.013 V. The emission profiles can vary both in amplitude and in time of peaking. The earliest peaking time observed in the figure is about 0.45 ms after breakdown in event no.24 and the latest is about 1.6 ms after breakdown in event no.5. The FWHM of the peaks ranges from about 0.5 ms(event no.4) to 1.8 ms(event no.12).

Events no.4 and no.8 followed the same pattern. In these two events, the signal intensity started to rise immediately after the breakdown, reaching a single peak value, and slowly decayed to zero. The intensity curves were smooth, with no sudden change in them. This

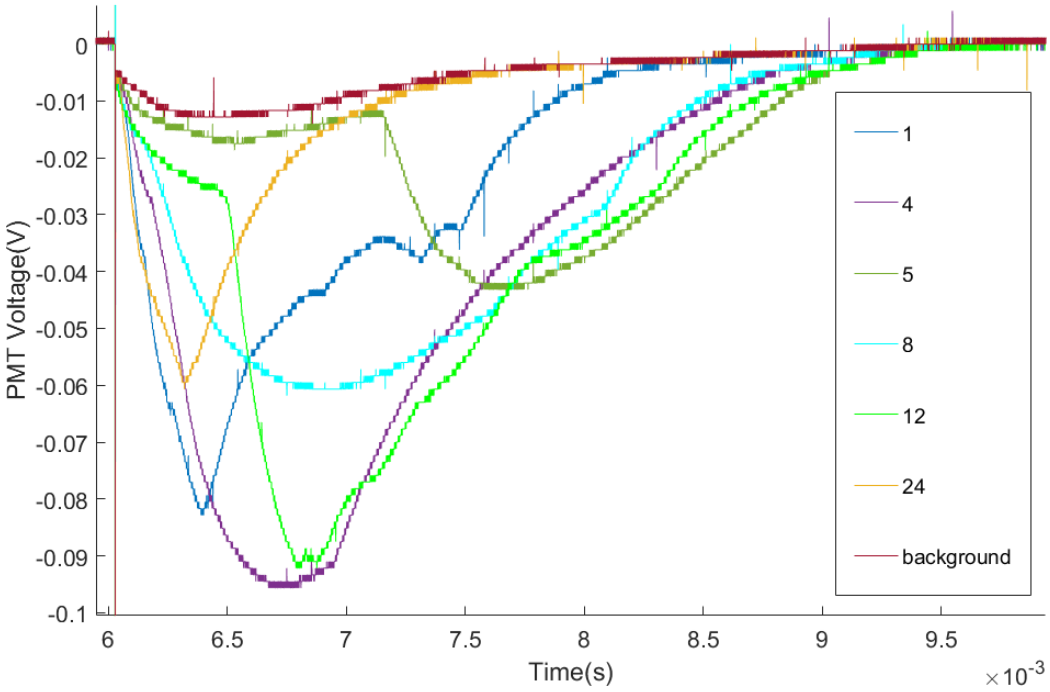

Figure 4.12: Spectrally filtered PMT signal curves of different sparks with cross flow introduced.

can be explained as the ordinary intensity trace of an event with nickel emission. Small molten pools of nickel were created by the breakdown, and the nickel was vaporized as a result of the heat effect. The vaporized nickel atoms then got excited by the plasma and emitted light which was collected by the PMT.

Events no.1 and no.24 share similar features. In these two events, the emission intensity rose immediately after breakdown, but reached the peak earlier than in event no.4, and peaked at lower values. After peaking, the intensity curves exhibit a sudden decrease, in comparison with the smooth variation in events no.4 and no.8. This results in lower FWHM of the peak.

In event no.5, another different pattern was observed. The PMT signal followed the background trace in the first microsecond after breakdown, which means no observation of nickel atoms in the plasma. At 1.1 ms after breakdown the rise in the PMT signal indicates that nickel emission started to appear in the spectrum. The decaying part of the signal followed the outline drawn by event no.4. Event no.12 showed similar characteristic as event no.5, but with a higher signal level before the appearing of nickel, and a steeper increase to a higher intensity of the nickel emission.

It is worth pointing out here that since this set of data was acquired when the spark gap was set to be horizontal, and the collective optics were arranged at an angle about the spark, some geometrical effect might affect the observation. There is a possibility that some light

was blocked by the platform holding the upper electrode. With this possibility considered, however, fig.4.12 can still show that the nickel emission in the sparks has a very random nature and that statistical approaches could be used to help promote understanding of the process.

4.3.2 Statistical measurements

To analyze the nickel emission statistically, an integral function of the oscilloscope was used. In this section, every data set consisted of 1000 data points, each representing the total emission intensity recorded from a single spark. The data points were acquired by calculating the integral of the PMT signal curves, as shown in fig.4.12, over time.

4.3.3 Inductive coil

The correlation of the energy charged into the ignition coil and the erosion of the electrode was studied first. As described in section 3.1, the charging time of the coil, thus the energy, is controlled by the width of the trigger pulse. 15 sets of data were recorded with the trigger pulse width ranging from 1 ms to 3 ms, and the repetition rate ranging from 2 Hz to 10 Hz. In fig.4.13, the average value of all PMT signal integrals in each data set was plotted.

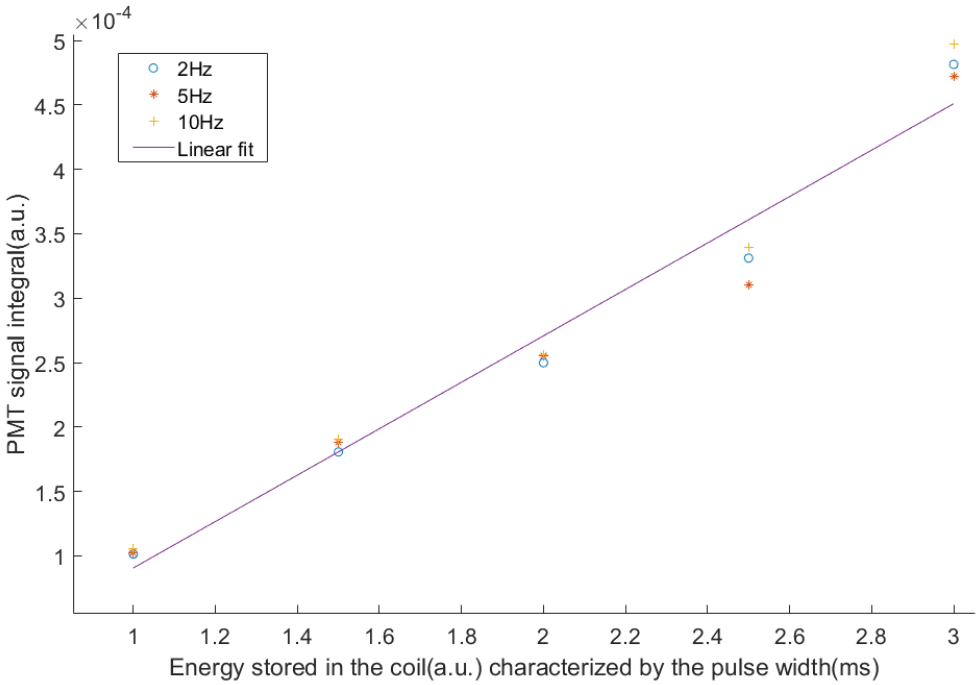

Figure 4.13: Averaged PMT signal integral as a function of trigger pulse width at different repetition rates.

A clear positive correlation can be seen between the emission signal and the energy stored in the coil. A longer trigger pulse dispatches more energy into the coil, thus more

energy into the discharge. In the voltage and current perspective, a longer trigger pulse prolongs the duration of the discharge and raises the secondary current. As a result of the increased energy in the discharge, more nickel atoms get evaporated and excited, which means the electrode suffers more erosion.

In the figure, some fluctuation caused by the variation of repetition rate can also be observed. However, as the repetition rate increased from 2 Hz to 10 Hz the averaged signal was observed to first decreased at 5 Hz and then increased at 10 Hz. Further investigation into the repetition rate's influence will be shown next. In fig.4.13, the three values with the same trigger pulse widths and different repetition rate were averaged, and a linear fit was done, as shown in the purple line. From the fit it can be seen that the dependence of the averaged signal on pulse width is almost linear. The correlation efficient of 0.984 also supported the conclusion.

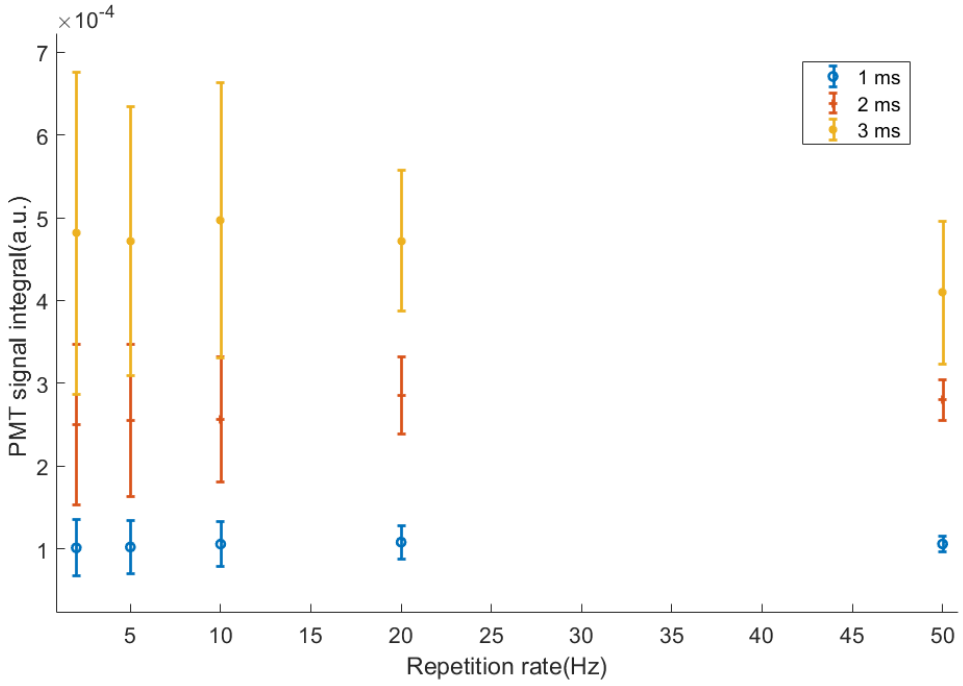

Figure 4.14: Averaged PMT signal integral and standard deviation as a function of repetition rate with different trigger pulse width.

In fig.4.14, the averaged signal and standard deviation of 15 data sets with pulse widths 1 ms, 2 ms, and 3 ms, and repetition rate ranging from 2 Hz to 50 Hz are plotted. Unlike the trigger pulse width, no clear correlation can be seen between the repetition rate and the averaged signal. But the decreased standard deviation in 20 Hz and 50 Hz cases indicates that a higher repetition rate may be able to help stabilize the discharge. By comparing the standard deviation of the 1 ms, 2 ms and 3 ms cases with the same repetition rate, another conclusion can be drawn that in discharges with higher energy the fluctuation in the erosion of the electrode tends to be larger than in low-energy discharges.

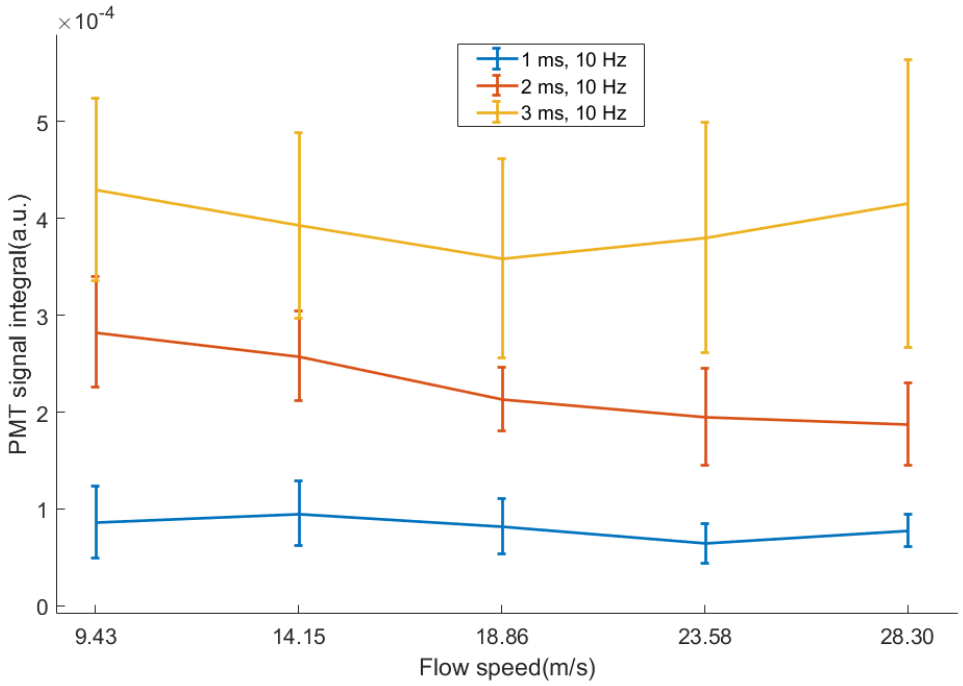

Figure 4.15: Averaged PMT signal integral and standard deviation as a function of flow speed, triggered with pulses with 1 - 3 ms width and 10 Hz repetition rate.

The influence of cross flow on the spark was studied and the results are shown in fig.4.15. The cross flow was nitrogen, sent out from a nozzle with a diameter of 1.5 mm. A float-type flow meter was used to measure the flow. Five different flow values were tested in the experiment, ranging from 1 L/min to 3 L/min with a step of 0.5 L/min. The corresponding gas velocity at the nozzle was calculated and marked in fig.4.15. In all cases, the spark was triggered with a repetition rate of 10 Hz.

From fig.4.15 it is observed that sparks with different trigger pulse width responded differently to the increasing flow velocity. In the 1 ms case, the signal reached a maximum at 14.15 m/s and minimum at 23,58 m/s. In the 2 ms case, the signal continued to drop with the increase in flow speed. And in the 3 ms case, the signal was similar when the flow speed is the highest and the lowest, and reached a minimum at 18.86 m/s. From these measurements it is concluded that erosion of the electrode is not related to the speed of the cross flow.

4.3.4 Modulated spark modes

In this section, 1000 sparks were measured for each of the 9 different spark modes. The spark modes were numbered from 1 to 9, and the description of the modes is listed in table 4.2. Corresponding voltage and current traces can be found in fig.4.1. All modes except the 200 mA 750 µs inductive mode were recorded under the same condition. The gain of

Table 4.2: Data set number and the corresponding spark mode

Data Set number	Spark mode
1	2 μF DC, single breakdown
2	2 μF AC, single breakdown
3	1 μF DC, triple breakdown, positive bias
4	1 μF DC, triple breakdown, negative bias
5	1 μF DC, triple breakdown, negative-positive-negative bias
6	2 μF AC, double breakdown
7	1 ms AC generated by five 1 μF capacitors
8	100 mA, 1300 μs inductive
9	200 mA, 750 μs inductive

the PMT was lowered in the 200 mA 750 μs case due to its extremely high signal intensity.

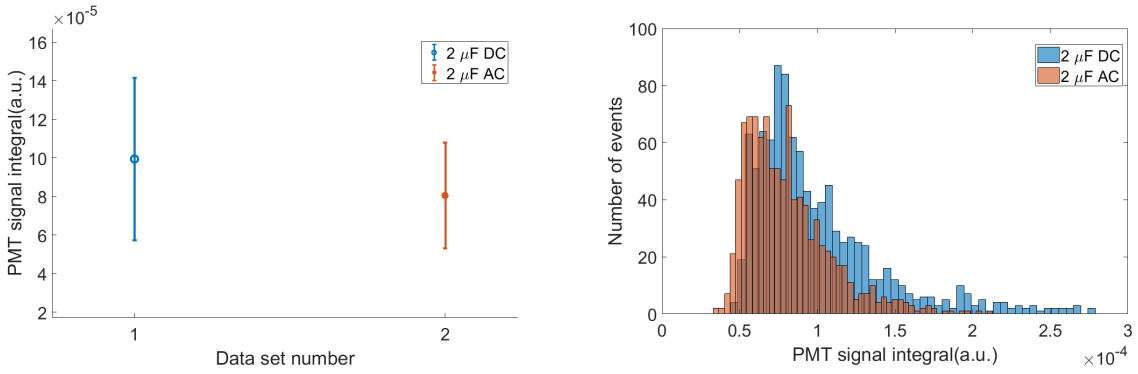

(a) (b)

Figure 4.16: Average values and standard deviations of PMT signal integrals calculated from 1000 2 μF negatively biased DC sparks(blue) and 1000 2 μF AC sparks(red) (a) and the corresponding histograms (b).

Figure 4.16 shows the comparison between the AC and DC capacitive modes with a 2 μF capacitor. From fig.4.16a the conclusion can be drawn that the DC mode, with a negative bias on the upper electrode, tends to erode the nickel electrode more than the AC mode. The average emission signal observed in the 1000 DC mode sparks was about 9.94 $\times 10^{-5}$. The erosion caused by the DC mode also tends to vary more widely than that of the AC mode. From the histograms, it can be seen that the AC mode was observed more often in the low-intensity region, but the difference is small. In about 10 sparks, the AC mode emitted intensity lower than the minimum intensity of the DC spark. Most intensities from the AC mode were distributed around 5.8 $\times 10^{-5}$, while most from the DC mode were distributed around about 7.7 $\times 10^{-5}$. The number of events that fell in the high-intensity region (above 1 $\times 10^{-4}$) in the DC data set is way larger than that in the AC data set. 32 events in the DC data set were observed to exceed the maximum intensity

in the AC data set.

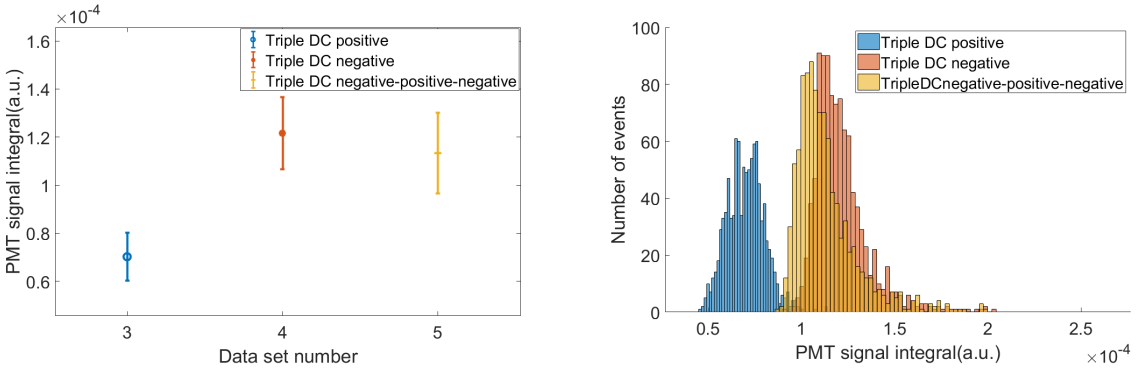

(a) (b)

Figure 4.17: Average values and standard deviations of PMT signal integrals calculated from 1000 1 μF DC triple breakdown sparks with positive bias(blue), negative bias(red) and negative-positive-negative bias(yellow) (a) and their corresponding histograms (b).

In fig.4.17, three DC modes with triple breakdown were compared, the difference among which being the bias applied on the Ir electrode. It can be seen from fig.4.17a that three positively biased breakdowns on the Ir electrode gave the least erosion on the Ni electrode, with an average signal of 7.0 $\times 10^{-5}$. The mode with three negative biased breakdowns gave the most erosion whose average signal was 1.2 $\times 10^{-4}$. The mode with two negative biased breakdowns and a positive one gave an average signal of 1.1 $\times 10^{-4}$, which is slightly lower than the signal of the negative biased case, but higher than the positive biased case. From this comparison a conclusion can be drawn that the Ni electrode suffers more erosion from evaporation when it acts as the anode. This can also explain why in the 2 μF capacitive modes less erosion was observed in the AC mode than in the DC mode: in the AC mode the nickel electrode acted as the cathode in 50% of the total operating time, during which it suffered a lower erosion rate than in the DC mode.

A difference can also be observed in the distribution of the signal intensities. In data set number 3 where all three breakdowns were positively biased(drawn in blue in fig.4.17b), the distribution was almost symmetric about the most probable intensity. About the same number of events were distributed in the low-intensity region and the high-intensity region. Whereas in the DC cases where the Ni electrode acted as the anode, as is shown in fig.4.16b in blue and fig.4.17b in red, the distribution extended to the high-intensity region more. A rough estimation can be made that in the negatively biased DC cases 50% of all events are distributed in the lower 25%-30% of the whole intensity range. Furthermore, a difference can be observed between the negatively biased DC data sets 1 and 4. Comparing the two histograms it can be seen that in the single breakdown case(data set 1) the distribution is more asymmetric than in the triple breakdown case(data set 4). More events in the single breakdown mode gave high emission signals.

Another comparison can be done between data sets 4 and 5. In data set 5, the second breakdown was positively biased, as opposed to the negatively biased in data set 4.

This resulted in a reduction in the number of events distributed in the 1.08-1.47 $\times 10^{-4}$ range, and an increase in the 0.90-1.08 $\times 10^{-4}$ range. The upper and lower limits of the distribution, however, were not observed to differ from each other by much.

A possible explanation may be found in the evaporation erosion model. In section 2.2.2, the erosion on the cathode was described. In [13], an effect was mentioned that the ionized copper atoms can move towards the cathode and be absorbed by the electrode. If the electrode is acting as the anode, however, the positively charged ions are less likely to be absorbed by the anode. This might contribute to the increased erosion. With this proposed, it is necessary to investigate more into the phenomenon for a final explanation.

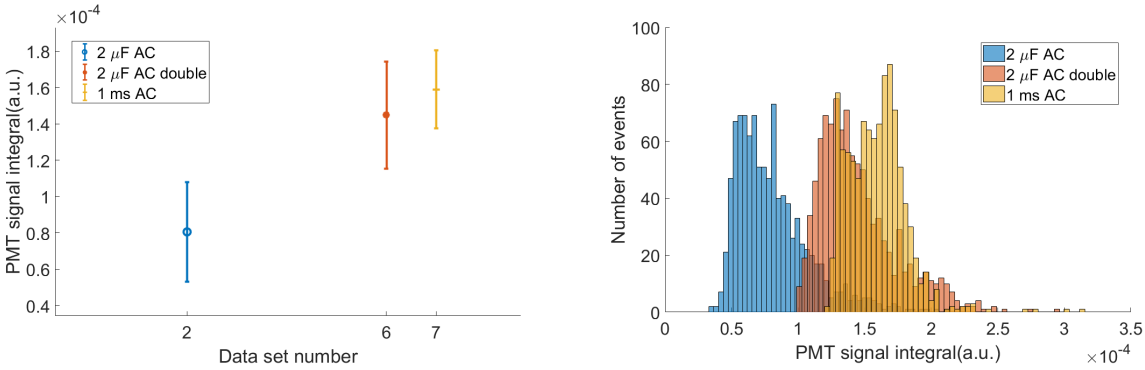

(a) (b)

Figure 4.18: Average values and standard deviations of PMT signal integrals calculated from 1000 2 μF AC single breakdown sparks(blue), 1000 2 μF AC double breakdown sparks(red) and 1000 1 ms sparks generated by consecutively firing 5 1 μF AC sparks(yellow) (a) and the corresponding histograms (b).

In fig.4.18, three data sets observing the AC sparks are shown. In fig.4.18a, it can be seen that the double breakdown 2 μF AC mode showed significantly more erosion signal than the single breakdown one, which is reasonable since in the double breakdown mode the electrodes experience two breakdowns and two sparks rather than one. However, the average signal of the double breakdown mode was 1.4 $\times 10^{-4}$, which is smaller than the signal of the single breakdown mode doubled. This indicates that the two discharges initiated consecutively with a short delay of about 500 μs behaved differently than two discharges separated with a delay of about 0.1 s would. From fig.4.18b it can be seen that the two data sets share a similar profile in distribution, the only difference being the intensity range.

The conclusion that two discharges would behave differently when triggered shortly after on another is not intuitive. Given the fact that there is only one group of data supporting this conclusion, more experiments are expected to be done in the future to further investigate the phenomenon and to produce possible explanation for it.

The third case shown in fig.4.18 is a 1 ms long AC spark. The spark duration was stretched by triggering five 1 μF capacitors consecutively. A detailed description was given

in section 4.1. From fig.4.18 it can be seen that the 1 ms AC mode eroded the Ni electrode more than the other two modes. In terms of signal intensity distribution, this mode behaved differently from all other modes. In this set of data, the most probable intensity lies in the higher intensity half of the intensity range. About 20 events were distributed in the range above 2 $\times 10^{-4}$, the relatively high-intensity region in the distribution, which is fewer than most other cases shown.

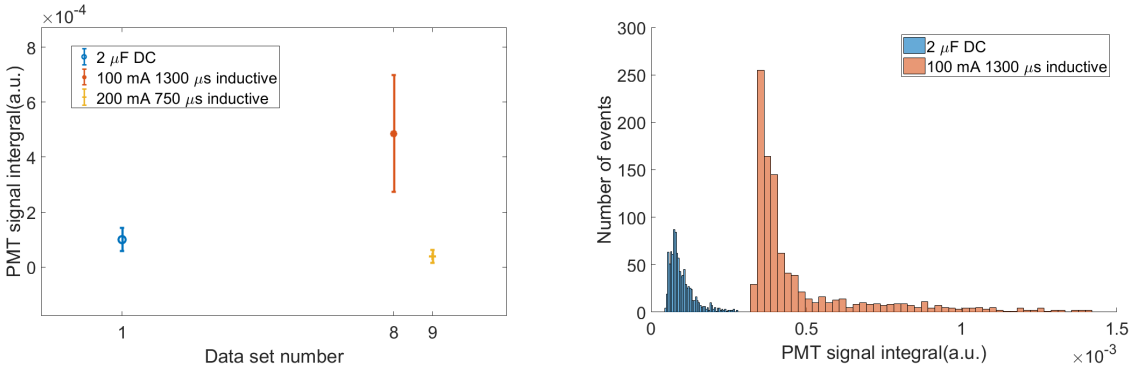

(a) (b)

Figure 4.19: Average values and standard deviations of PMT signal integrals calculated from 1000 2 μF AC single breakdown sparks(blue), 1000 inductive sparks with 100 mA secondary current lasting 1300 μs(red) and 1000 inductive sparks with 200 mA secondary current lasting 750 μs(yellow) (a) and the corresponding histograms of the first two cases (b).

In fig.4.19, the average and standard deviation of the signals from two inductive modes whose secondary current was held at a certain level for a period of time are shown. The data on the 2 μF DC data set was plotted as a baseline of comparison. Clearly, by holding the current at a constant level, significantly more energy was dispatched into the discharge, and as a result the erosion on the Ni electrode was also raised to a dramatically high level. Note that in the 200 mA 750 μs case the gain of the PMT must be reduced to 0.179 V from the 0.231 V used in all other measurements, to protect the PMT from being burnt. The actual signal was even higher than the 100 mA 1300 μs case. For this reason the histogram of this case was not plotted, as it is not comparable with the others.

From the histogram, it can be seen that the distribution of the 100 mA case was much wider. The intensities ranged from 3.2 $\times 10^{-4}$ to 1.4 $\times 10^{-3}$. The weakest signal observed in the 200 mA 750 μs mode was stronger than the strongest in the 2 F DC mode; the relatively strong events in the inductive mode can be one order of magnitude stronger than those in the capacitive mode. The histogram further proved that the modes with constant secondary current can erode the electrode quicker than those whose secondary current decayed during the spark duration.

4.4 High-speed imaging

In this section, the high-speed imaging results are shown. Three different settings were used in the measurements. When no filter was used, the gate width of the intensifier was 150 ns and the gain was 519.9; when the long-pass filter was applied, the gate width was 200 ns and the gain was 540.2; with the band-pass filter the numbers were 1.0 μs and 649.9. The images shown in the thesis were bit-shifted by 2 bits to increase the contrast for better readability. The positioning of the electrodes is shown in fig.4.4. Due to the movement of the equipment the field of view is the same as shown in fig.4.4 in the band-pass filtered cases. Minor difference exits in other cases. The diameter of the Ni electrode was measured to be 2.45 mm, and the Ni electrode takes 161 pixels in fig.4.4. Thus the estimated imaging ratio is about 15.2 μm/pixel. In all cases shown in this section, the Ir electrode was negatively biased, making the Ni electrode the anode.

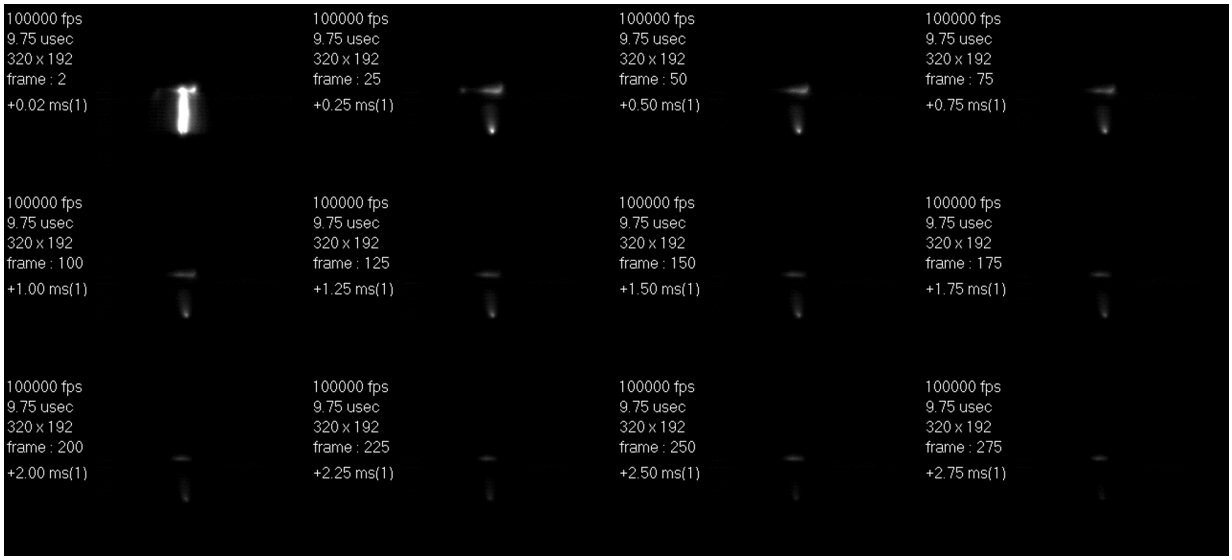

Figure 4.20: High-speed imaging sequence of a spark without spectral filtering.

An imaging sequence of a discharge with no spectral filtering is shown in fig.4.20. In frame 2, a bright channel is observed, connecting the anode and the cathode. This is the plasma channel created by the breakdown. The intensity of the breakdown is higher than any following moments during the discharge, but the lifetime of the phase is short. The fact that the channel cannot be observed in frame 3(not shown in the figure) indicates that the lifetime of the breakdown is shorter than 10 μs, which is the period of the imaging sequence.

Following the breakdown, the shape of the discharge was stabilized. Lacking the method to measure the cathode drop, it could not be determined if the discharge was in the arc phase or glow phase, but a difference can be seen between the breakdown and the following phase. In the discharge, after breakdown, a relatively large area of the Ir electrode was glowing. In frame 25, light was observed on almost all the Ir electrode. In contrast, the

emission on the Ni electrode is always observed on one concentrated spot. The strongest signal was observed on the Ni electrode; the channel grew wider and dimmer as it extended to the Ir electrode. A narrow band can be observed near the Ir electrode where no emission was recorded. In multiple imaging sequences, it can be concluded that the emission channel always started on the edge of the Ir electrode.

As the discharge goes into its later phase, the shape of the discharge remains unchanged, but the intensity gradually decreases. A decrease in the emitting area on the Ir electrode can also be observed. The bright spot on the Ni electrode seemed to fade quicker than the Ir electrode.

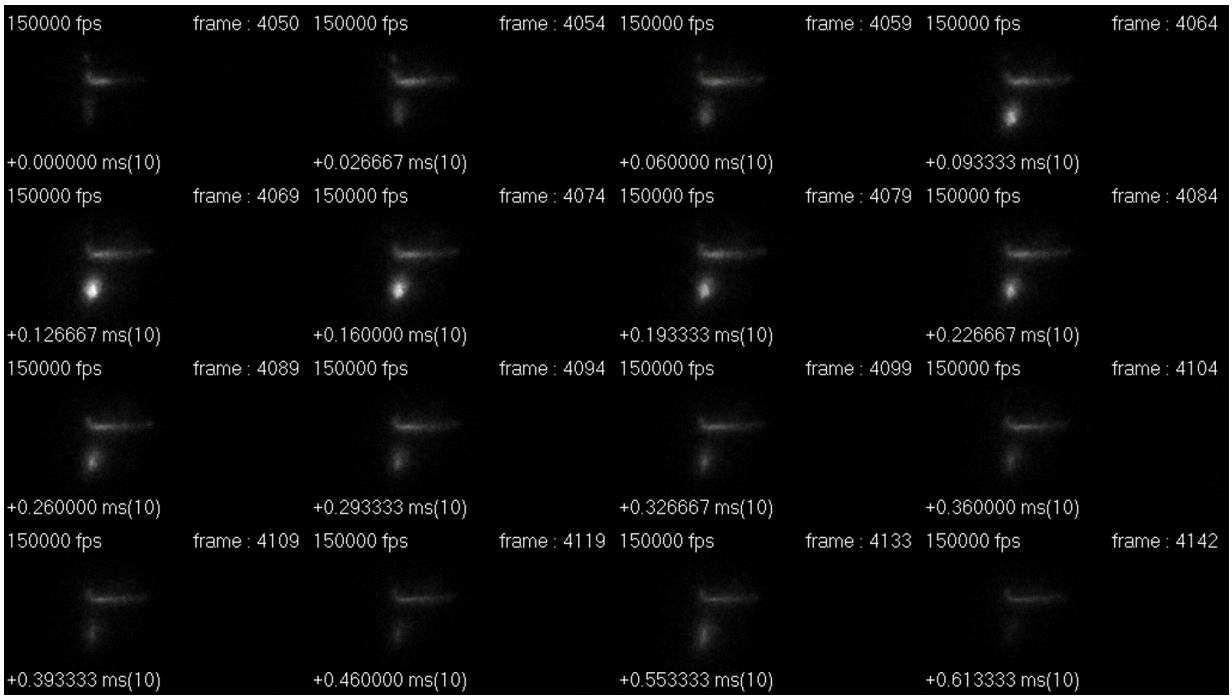

Figure 4.21: High-speed imaging sequence of a discharge with high Ni emission, recorded with a 343 nm, 10 nm FWHM band-pass filter.

Using a 343 nm band-pass filter, the temporal and spatial properties of the Ni emission was studied, and one of such imaging sequences is shown in fig.4.21. It can be seen here that in this discharge the plasma channel appeared on the left side of the Ir electrode, and landed on the Ni electrode also to the left. This explained the difference in the position of the emission lines observed in spectra shown in fig.4.5a and 4.5b.

In the spectrally filtered images, the discharge had a similar structure as in the unfiltered ones. The frames shown in fig.4.21 covered a time window of about 0.61 ms after breakdown. The representative frames of this phase can be found in frames 25 and 50 in fig.4.20. In the unfiltered images, the change in intensity during this period of time is minor, almost unrecognizable. In the filtered images, the emission intensity near the Ir electrode can be observed to be relatively stable. Near the Ni electrode, however, an

increase in intensity can be seen, indicating the existence of excited Ni atoms. From the images it can be concluded that the intensity of the Ni emission increased peaked at about 0.13 ms after breakdown, and continued for about 0.6 ms until the intensity reached 0. A small rise in intensity can be seen at about 0.55 ms. As shown in the figure the Ni atomic emission can be observed only in a region near the Ni electrode. Based on the spectral measurements near the Ir electrode, the glowing area on the Ir electrode can be identified as a background emission. Taking into consideration the scale of the images, the area where Ni emission was observed can be estimated to be about 0 - 0.35 mm above the Ni electrode, while the whole electrode gap was about 0.5 mm.

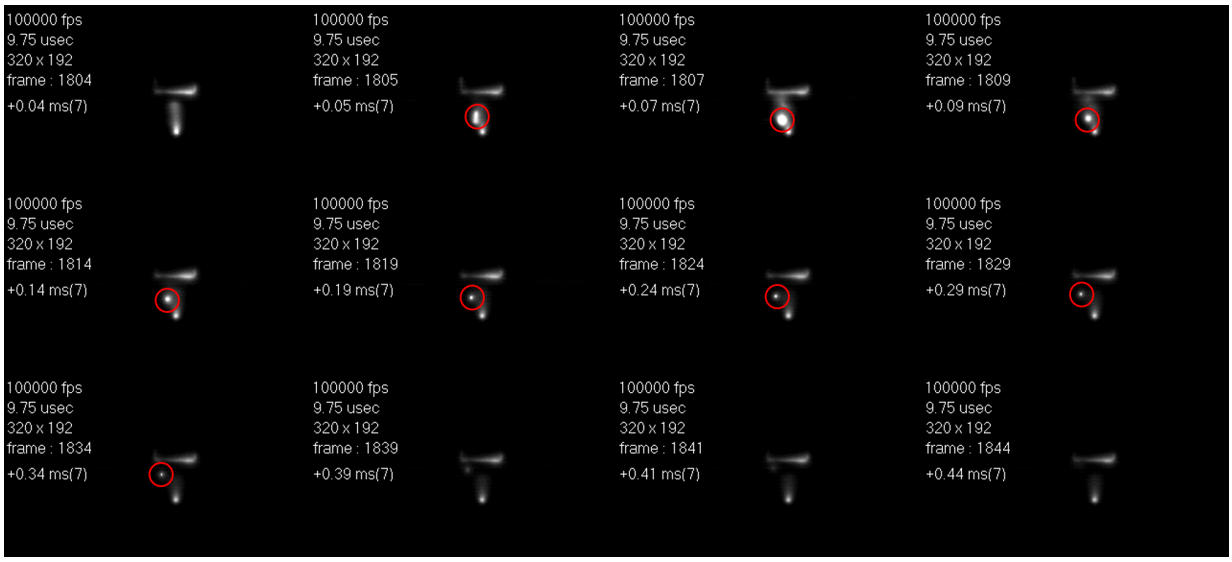

Figure 4.22: High-speed imaging sequence of a bright spot leaving the plasma channel, as marked in the red circle, recorded with no filtering.

In rare cases, a small bright spot can be seen generated in the plasma channel and leaving it. Fig.4.22 shows one of such cases recorded with no spectral filtering. In frame 1805, along the plasma channel a bright area appeared, which in the following frames was observed to be two separate spots. The spot on the top moved up towards the Ir electrode and disappeared at frame 1816. Comparing frames 1809 and 1819 it can be seen clearly that the dark area near the Ir electrode was lightened by the spot in the former frame. The second spot behaved differently from the first one. In the first 0.06 ms of its appearance, its position remained unchanged, but both its intensity and volume increased, maximizing at frame 1807, which is 0.07 ms after breakdown. The spot then moved left leaving the plasma channel, and in the same time drifted towards the Ir electrode. The spot disappeared at frame 1844, 0.44 ms after breakdown.

The appearance of the bright spots can be potentially due to the particle ejection erosion described in section 2.2.1. But due to both the lack of spectral information and more observation of such events it is hard to draw a solid conclusion. More investigation is required to understand this phenomenon.

4.5 Macro imaging of the electrode

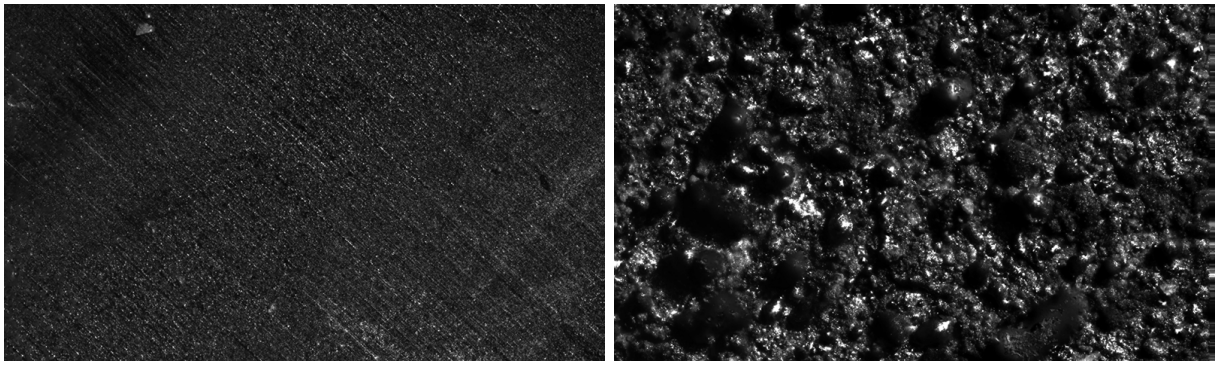

(a) (b)

Figure 4.23: Macro imaging of the surface of a new Ni electrode (a) and the electrode used in the experiments (b).

In this section, two macro imaging photos were taken, one on a new spark plug electrode made from Ni, and the other on the worn Ni electrode used in the experiments, to provide a basic impression of the erosion. The photos are shown in fig.4.23. Fig.4.23a was stacked from 10 photos with a step length of 0.01 mm; fig.4.23b was stacked from 11 photos with the same step length.

In fig.4.23a, the surface of the new electrode was observed to be flat and even. The parallel lines in the photo are due to the machining of the surface. In the original photo series, the in-focus area is observed to move evenly from the left of the area of interest to the right. This proves that the original electrode surface is flat, and the out-of-focus areas are only present because the electrode was not placed perfectly parallel to the camera's imaging plane.

Fig.4.23b shows the damaged electrode surface of the Ni electrode used in the experiments. The electrode had been run for no less than 200 hours, and severe deformation of the flat, uniform surface it originally had was observed. In the region recorded in the figure, multiple bulges are observed. Judging from the original images the height difference can be as much as 80-90 μm. The diameter of the large bulges are typically 90-100 pixels, which corresponds to about 52-58 μm. Other than the large bulges small bumps can also be observed on the electrode surface whose height is 10 μm or less.

5 Conclusion and outlook

5.1 Summary

Multiple detection approaches have been applied in the study on electrical discharge in spark plugs, and a feasible method able to investigate the temporal behavior of erosion on Ni electrodes has been proposed and utilized.

Spectroscopic measurements on the spectral region centered at 350 nm revealed the existence of three nitrogen emission bands in discharges in air: N_2 C-B (0,0) at 337.0 nm ,C-B (0,1) at 357.6 nm and C-B (1,2) at 353.6 nm. In the meantime, a random appearance of Ni atomic emission lines between 338 nm and 355 nm was also observed. Randomness also lied in the position of the strong spectral signal.

Based on the spectroscopic measurements, a PMT detection approach was proposed. A band-pass filter centered at 343 nm with a 10 nm FWHM was put in front of a PMT to serve as the erosion detector. The validity of the approach was studied by comparing the histogram of the intensity of a single Ni emission peak with the histogram of the summed intensity in the selected spectral region.

Having validated the approach, studies were carried out on different spark modes with it. Time-resolved measurements revealed a delay between the breakdown and the peak intensity of Ni emission, ranging from 0.3 ms to 1.5 ms. By calculating the integral of the PMT signal, a statistical study on the erosion characteristics was enabled. It was found that in the inductive ignition system the erosion is mostly affected by the charging time of the coil. Effects of repetition rate and cross-flow speed were also investigated, but no correlation was found. In the capacitive system, results showed that AC sparks caused less erosion than DC sparks and that Ni electrodes suffer more erosion when acting as the anode. It was also found that two breakdowns triggered with a small separation may cause less erosion than two breakdowns triggered with a large separation.

It should be mentioned that the proposed detection approach has several limitations. A major limitation is that this method is limited to Ni electrodes and applying the same technique to other metal can be not trivial. Another limitation is the lack of knowledge in the ratio between ground state Ni atoms and excited Ni atoms. This means that without further data the method proposed here can only be used qualitatively. A third limitation is that this method only detects Ni atoms in the gas phase. The erosion caused by particle ejection, for example, can not be detected by this method. One possible approach to detect the particle ejection is laser-based scattering detection.

High-speed imaging was also used in the study of the discharge. Unfiltered high-speed imaging sequences revealed the shape of the plasma channel. A spectral filter same as used in the PMT measurements was applied in the high-speed imaging, and the results showed that the Ni emission in the discharge was confined in a region near the Ni electrode. In rare occasions, bright spots were observed to fly away from the plasma channel in unfiltered images, and the reason remained unknown.

Finally, a photo of the worn electrode was taken, using a self-built macro imaging system, to compare with one of a new electrode. The morphology of the electrode erosion

was observed.

5.2 Outlook

As previously mentioned there are limitations on the proposed detection method. In the future, more investigation may be done in the study on excitation of the Ni atoms in the plasma, and also on the detection of erosion processes that don't produce free metal atoms.

Due to the limitation in the test rig, more parameters that are relevant in the electrical discharge process remain untested. Examples of such parameters include pressure and temperature of the surrounding gas, species of the gas, and temperature of the electrode. It is also necessary to do tests in real engine environments.

Some phenomena observed in this thesis work, for example the difference in erosion when the Ni electrode acts as the cathode and the anode, are to be explained. Further studies are still needed. The ultimate goal of relevant work would be to try to modify either the spark plug design or the ignition system, to reach the desired lifetime of spark plugs.

References

[1] Yuri P Raizer. Gas discharge physics. 1991.

[2] Myung Jun Lee, Matt Hall, Ofodike A Ezekoye, and Ronald D Matthews. Voltage, and energy deposition characteristics of spark ignition systems. Technical report, SAE Technical Paper, 2005.

[3] Rudolf Maly. Spark ignition: its physics and effect on the internal combustion engine. In *Fuel economy*, pages 91–148. Springer, 1984.

[4] Akio Katoh and Keiji Kanao. Long life spark plug having minimum noble metal amount, November 23 1999. US Patent 5,990,602.

[5] Hua-Tay Lin, Michael P Brady, Roger K Richards, and DM Layton. Characterization of erosion and failure processes of spark plugs after field service in natural gas engines. *Wear*, 259(7-12):1063–1067, 2005.

[6] Hibiki Ryuzaki. A study on mechanism of gas engine spark plug deterioration. In *Proceedings of IGRC 2008*, pages 3046–3060, October 1996.

[7] S Javan, SV Hosseini, SS Alaviyoun, and F Ommi. Effect of electrode erosion on the required ignition voltage of spark plug in cng spark ignition engine. *The Journal of Engine Research*, 26(26):31–39, 2012.

[8] Saeed Javan, Syed Shahabodin Alaviyoun, Seyed Vahid Hosseini, and F Ommi. Experimental study of fine center electrode spark plug in bi-fuel engines. *Journal of Mechanical Science and Technology*, 28(3):1089–1097, 2014.

[9] Sebastian Różowicz. Use of the mathematical model of the ignition system to analyze the spark discharge, including the destruction of spark plug electrodes. *Open Physics*, 16(1):57–62, 2018.

[10] David Alexander Staack. Characterization and stabilization of atmospheric pressure dc microplasmas and their application to thin film deposition. 2009.

[11] Eoin W Gray and Julian R Pharney. Electrode erosion by particle ejection in low-current arcs. *Journal of Applied Physics*, 45(2):667–671, 1974.

[12] Jacques A Augis, FRANK J GIBSON, and Eoin W Gray. Plasma and electrode interactions in short gap discharges in air ii. electrode effects. *International Journal of Electronics Theoretical and Experimental*, 30(4):315–332, 1971.

[13] Sylvain Coulombe and Jean-Luc Meunier. Importance of high local cathode spot pressure on the attachment of thermal arcs on cold cathodes. *IEEE transactions on plasma science*, 25(5):913–918, 1997.

[14] Sylvain Coulombe and Jean-Luc Meunier. Theoretical prediction of non-thermionic arc cathode erosion rate including both vaporization and melting of the surface. *Plasma Sources Science and Technology*, 9(3):239, 2000.

[15] Peter Sigmund. Theory of sputtering. i. sputtering yield of amorphous and polycrystalline targets. *Physical review*, 184(2):383, 1969.

[16] KK Hamamatsu Photonics. Photomultiplier tubes: Basics and applications. *Edition 3a*, 310, 2007.

[17] Triveni Rao and David H Dowell. An engineering guide to photoinjectors. *arXiv preprint arXiv:1403.7539*, 2014.

[18] Bahaa EA Saleh and Malvin Carl Teich. *Fundamentals of photonics*. john Wiley & sons, 2019.

[19] Joseph Ladislas Wiza et al. Microchannel plate detectors. *Nucl. Instrum. Methods*, 162(1-3):587–601, 1979.

[20] Thierry Gys. Micro-channel plates and vacuum detectors. *Nuclear Instruments and Methods in Physics Research Section A: Accelerators, Spectrometers, Detectors and Associated Equipment*, 787:254–260, 2015.

[21] Munir El-Desouki, M Jamal Deen, Qiyin Fang, Louis Liu, Frances Tse, and David Armstrong. Cmos image sensors for high speed applications. *Sensors*, 9(1):430–444, 2009.

[22] Alan Hoffman, Markus Loose, and Vyshnavi Suntharalingam. Cmos detector technology. *Experimental Astronomy*, 19(1-3):111–134, 2005.

[23] Craig J Sansonetti, Marc L Salit, and Joseph Reader. Wavelengths of spectral lines in mercury pencil lamps. *Applied optics*, 35(1):74–77, 1996.

[24] Jean E Sansonetti and William Clyde Martin. Handbook of basic atomic spectroscopic data. *Journal of Physical and Chemical Reference Data*, 34(4):1559–2259, 2005.

[25] Wooyeong Kim, Choongsik Bae, and Olaf Toedter. Spatio-temporally resolved emission spectroscopy of inductive spark ignition in atmospheric air condition. In *Ignition Systems for Gasoline Engines*. IAV, 2018.